



# High-resolution X-ray spectroscopy of astrophysical plasmas with X-ray microcalorimeters

Yuichiro Ezoe<sup>1</sup> · Takaya Ohashi<sup>1</sup> · Kazuhisa Mitsuda<sup>2</sup>

Received: 18 March 2019 / Accepted: 22 May 2021 / Published online: 14 June 2021  
© The Author(s) 2021

## Abstract

High spectral resolution with a resolving power,  $E/\Delta E \gtrsim 1000$  at 6 keV, is now available in X-ray astronomy. X-ray observations are particularly effective for plasma studies since major atomic transitions appear as spectral features in the X-ray band. High-resolution spectroscopy enables us to probe a wide variety of astrophysical plasmas, which are not obtainable from ground experiments, regarding their temperature, density, magnetic field, gravity, and velocity. In this review, we describe what are the X-ray emitting plasmas in the Universe, along with basic plasma diagnostics, and depict historical development of the techniques used for the X-ray spectroscopy. We outline the X-ray microcalorimeter instrument, soft X-ray spectrometer (SXS), onboard the ASTRO-H satellite. Despite the short lifetime of the satellite in orbit for about a month, observations with the SXS have shown the remarkable power of high-resolution spectroscopy in X-ray astronomy. Observed spectrum of the hot plasma in the core region of the Perseus cluster showed He-like Fe K-line to be clearly resolved into resonance, forbidden and intercombination lines for the first time. The line width indicates that the turbulent pressure amounts to only 4% of the thermal pressure of the plasma. We also describe new findings and constraints obtained from the superb spectrum of the Perseus cluster, which all indicate a great potential of X-ray spectroscopy. The recovery of the spectroscopy science of ASTRO-H is aimed at with XRISM, a Japanese mission planned for launch in early 2020s. In further future, Athena will expand the rich science with its high sensitivity and spectral resolution in early 2030s.

**Keywords** High-energy astrophysics · X-ray · Microcalorimeter

---

✉ Yuichiro Ezoe  
ezoe@tmu.ac.jp

<sup>1</sup> Tokyo Metropolitan University, 1-1 Minami-Osawa, Hachioji, Tokyo 192-0397, Japan

<sup>2</sup> Japan Aerospace and exploration Agency (JAXA), The Institute of Space and Astronautical Science (ISAS), 3-1-1 Yoshinodai, Chuo, Sagamihara 252-5210, Japan

## 1 Introduction

This review describes basic properties of astrophysical plasmas, and shows how high-resolution X-ray spectroscopy can effectively bring us their detailed information.

Plasmas are not commonly found on Earth, where ordinary matter has typical temperatures much lower than the level which causes ionization. However, when one goes into the Universe, plasmas are the most natural form of the matter existence. Plasmas prevail in stars, hot interstellar medium in many galaxies including our Galaxy, and hot intergalactic medium filling clusters of galaxies. Also, there are collapsed objects, such as white dwarfs, neutron stars, and black holes of largely different masses, and these objects can be studied by observing plasmas which fall into and/or flow out from their deep potential well. Even the upper atmosphere of Earth and other planets consists of plasmas.

X-rays are high-energy photons in the energy range from 0.1 keV to a few tens of keV, and are produced preferentially in hot objects with temperatures in the range  $10^6 - 10^8$  K, where matter takes the form of plasmas. These are, in fact, the temperatures of cosmic plasmas which exist in wide categories of cosmic objects mentioned above. This makes X-rays the most efficient waveband to probe the physical properties of plasmas. Observational study of cosmic plasmas with X-rays has several different dimensions: image, energy, time, and polarization. Among them, the energy dimension, namely the spectroscopic capability, has shown a great progress in recent years, due much to the X-ray microcalorimeters coming into play. We will focus on this technique and describe initial results obtained by ASTRO-H in the later half of this review.

We note that  $\gamma$ -rays, with energies greater than 100 keV, can further probe non-thermal processes or nuclear reactions taking place in the Universe, and will grow up to be a rich field when the sensitivity will be substantially improved in future.

This paper is organized as follows. First, we describe the basics of astrophysical plasmas relevant for the X-ray study, followed by key features obtained from X-ray spectroscopy observations and a brief history of instrument development of X-ray spectroscopy. We depict the X-ray microcalorimeter instrument SXS (Soft X-ray Spectrometer), onboard the ASTRO-H (Hitomi) satellite, and report scientific highlights from the SXS observations. Finally, we outline future prospects with X-Ray imaging spectroscopy mission (XRISM), which is the recovery mission of ASTRO-H carrying the X-ray microcalorimeters, and the large observatory Athena led by ESA.

## 2 Astrophysical plasmas

### 2.1 Overview of astrophysical plasmas

Astrophysical plasmas can be found in almost all categories of objects in the Universe. In fact, as large as about 80% of baryons in the universe are considered to be in the form of hot plasmas with temperatures in the range  $10^6 - 10^8$  K Fukugita et al. (1998), Branchini et al. (2009). These plasmas partly reside in clusters of galaxies, and, for the most part, along large-scale structure of the Universe which is yet to be fully explored. Atmospheres of normal stars have temperatures in 3000–20,000 K and are ionized, often accompanied by coronae above the photosphere with temperatures of million K or more. The heating mechanism of the corona, namely how stellar atmosphere of a few thousand K can produce million K plasmas above it, is still an important question under study Sakurai (2017). Supernova and their remnants are also filled with hot plasmas with typical temperatures between  $10^6$  and  $10^8$  K. Material falling onto collapsed stars, i.e. white dwarfs, neutron stars and black holes, forms an accretion disk whose innermost region becomes very hot and radiates X-rays. Therefore, X-ray study of astrophysical plasmas enables us to directly look into the formation and evolution processes of these plasmas which are under very different conditions from those available from the ground experiment.

General properties of astrophysical plasmas are shown in Fig. 1, in which electron density and temperature for various astrophysical plasmas are plotted. The electron density ranges 40 orders of magnitudes, and the temperature spans 6 orders: indicating the immense richness of plasma properties in the Universe. X-rays are emitted

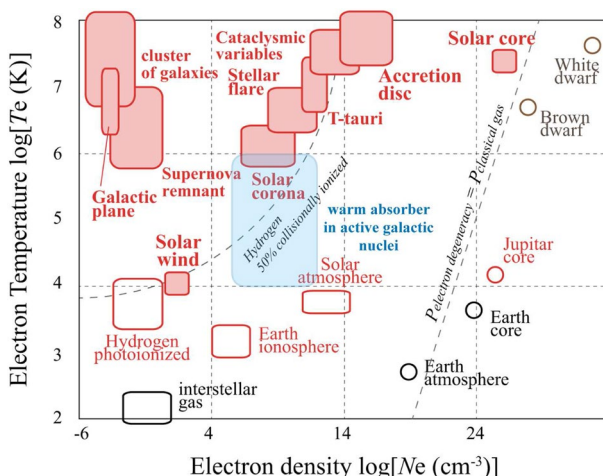
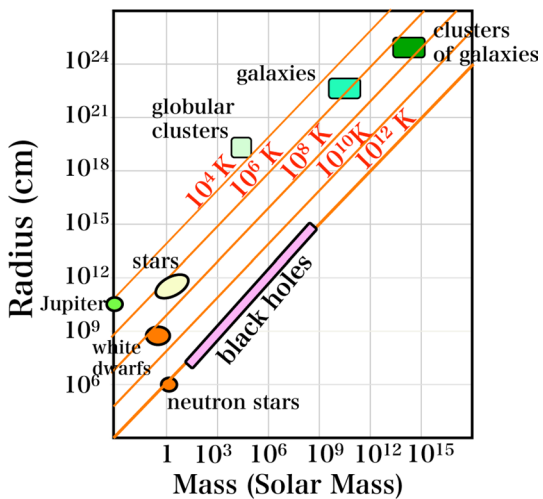


**Fig. 1** Various astrophysical plasmas plotted on a plane of electron density and electron temperature. Filled squares represent highly ionized plasma, whereas open red ones depict weakly ionized or high-density plasma. Black-blue symbols indicate neutral material and photo-ionized plasma. Revised from the original figure in ASTRO-H CookBook Members (2015)

**Fig. 2** Average temperature of self-gravitating systems in the Universe based on the virial theorem. Orange lines indicate constant temperature. Revised from the original figure in Makishima (2008)



from ionized plasmas with electron temperature ranging from  $10^6$  to  $10^8$  K and electron density from  $10^{-5}$  to  $10^{14}$  cm $^{-3}$ . These plasmas are not always under thermal equilibrium, since heating and cooling (and hence ionization and recombination) processes go very slowly when the particle density is low, as indicated in Fig. 2, and the spatial scale is large. The largest example is clusters of galaxies, encompassing a typical diameter of  $10^7$  light years. Photoionization is a major ionizing mechanism for plasmas near bright X-ray objects, and the ionization equilibrium (distribution of ionization degree) is very different from the case of collisional ionization case. As described later, charge exchange is another basic process which enables us to examine interaction between ionized particles and neutral gas even in a very low density environment. X-ray spectroscopy can characterize physical properties of most of the plasmas shown in Fig. 1, as depicted for some cases later.

For optically thin plasmas under collisional ionization or photo-ionization, their X-ray spectra consist of line and continuum components. The continuum emission is generated via thermal bremsstrahlung, radiative recombination, and two photon decay of metastable states, as described later. The continuum X-ray spectrum tells us the electron temperature and the emission measure  $EM = n_e n_H V$  at a given temperature where  $n_e$  and  $n_H$  are the number densities of electrons and protons, respectively, and  $V$  is the emitting volume. Using geometry assumption and  $n_H \sim 0.85 n_e$  for a fully ionized plasma, we can determine the electron density. The electron temperature and density are key parameters to characterize the plasma itself and its environment. Combined with imaging data, we can figure out how plasmas undergo heating and cooling down to the actual physical processes such as compressional or shock heating and radiative or expansion cooling, for example. The presence of the recombination continua in the spectrum immediately tells us that electrons are much cooler than what is expected from the ionization states of ions. We can also tell whether the plasma is at least partially surrounded by cold matter by measuring absorption lines and edges. Emission lines are produced when transitions of electrons from high to low levels occur in specific elements, and the precise energy of the line center would tell us which level of

which element is involved. The center energy, intensity and width of the line spectrum allow us to determine many parameters: chemical abundance, turbulent or bulk motion of the plasma, plasma density, matter thickness in the line of sight, and ion temperature (via the line width). These points will be further addressed in later sections.

## 2.2 Hot plasmas

As mentioned earlier, a variety of heating or ionization processes work in cosmic sources. The heating mechanisms involve gravity, magnetic field, explosion, jet formation, rotation, collision, external radiation, as well as charge exchange process. Here, we pick up the gravitational heating of plasmas, since it is a very common process operating in galaxies, in clusters of galaxies, around supermassive or stellar-mass black holes, and around collapsed stars such as white dwarfs and neutron stars. We note that the gravitational heating is the most useful mechanism with which we can study the presence and spatial distribution of the dark matter.

Hot plasmas with somewhat narrow temperature range  $kT = 10^6 - 10^8$  K are commonly observed from a number of objects, such as compact stars, hot interstellar medium, starburst and elliptical galaxies, and clusters of galaxies, even though their mass and spatial scale are very much different. These plasmas are either heated or confined by gravity and usually in collisional ionization equilibrium (CIE). Gravitational heatings usually operate through contraction of self-gravitating systems or accretion of matter to a deep potential well. In such processes, half of the gravitational potential energy is released as X-ray radiation, whereas the other half becomes internal energy of the accreting matter. Hence, the accreting matter emits X-rays and becomes hot at the same time. This two-way distribution of the potential energy is governed by the virial theorem, and the fifty-fifty distribution is resulted from the  $r^{-1}$  dependence of the gravitational potential.

Figure 2 shows average temperatures estimated from the virial theorem for a number of self-gravitating systems. For compact objects, matter falls into the gravitational potential with small radii, and strong heating is caused by the high ratio of the stellar mass over the radius. Note that the temperatures we observe in these compact objects are often different from their virial temperature because their emission is optically thick (except those from white dwarfs) and strongly affected by cooling. On the other hand, hot plasmas in galaxies and clusters of galaxies are characterized by lower temperature than in compact objects and their emission is optically thin. This is due to their large spatial sizes, despite their large aggregate mass. Nevertheless, temperatures in these systems can reach  $\sim 10^{7-8}$  K which is suitable for X-ray spectral observations. Thus, the relatively narrow range of the mass to radius ratio is resulted, making X-ray measurement to be very effective for such a wide range of plasmas in these objects.

## 2.3 Ionization conditions

Atoms are ionized when the temperature reaches more than a few 1000 K. However ionization can occur even under low temperature conditions. To distinguish the ionization condition of plasmas precisely, four different temperatures are defined; (1)

the electron temperature  $T_e$ , (2) the kinematic ion temperature  $T_i$ , normally referred to as “ion temperature” in plasma physics, (3) the excitation temperature  $T_{ex}$ , which is strongly coupled with  $T_e$ , and (4) the ionization temperature  $T_z$  of heavy ions. As mentioned later,  $T_z$  should approach  $T_e$  in time when collisions are the dominant ionization process.

The simplest case is a plasma in CIE, as observed in, e.g., stellar coronae and intracluster medium in clusters of galaxies. Under CIE, all four temperatures are the same:  $T_e = T_i = T_{ex} = T_z$ .

In plasmas under ionization equilibrium (not necessarily in CIE), distribution of ionization degree for respective elements is determined by a balance between ionization and recombination. Ionization will advance through collision, photoionization, shocks and compressional heating. Recombination process includes radiative recombination, collision, or through adiabatic expansion. The ionization equilibrium is described by fractional distribution of ionization states for each element, and it depends on the actual mechanism of ionization and recombination. As an example, Fig. 3 shows diagrams for O and Fe ions under collisional ionization equilibrium as a function of electron temperature. He-like ions ( $O^{+6}$  and  $Fe^{+24}$ ) are stable and indicate high abundance for a wide range of electron temperature. X-ray spectral features, such as emission or absorption lines and recombination edges for different species, enable us to constrain the distribution of ionization degree, along with electron temperature and chemical abundance of the plasma. Conventional evaluation has been carried out by generating a model spectrum for assumed set of

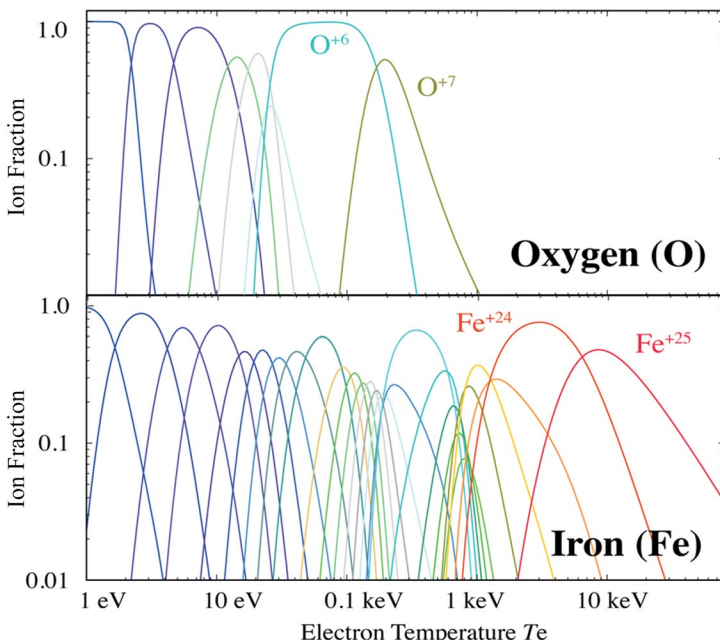


**Fig. 3** Ion fraction for gas in collisional ionization equilibrium as a function of electron temperature ASTRO-H CookBook Members (2015). Different colors correspond to different ionization states

parameters, which will then be fitted to the observed one until the best-fit parameters are obtained. Such a spectral fit is a common practice in estimating physical parameters of plasmas. With high spectral resolution, like the one with microcalorimeters, we may derive the plasma parameters based only on the line features (center energies, intensities, widths and shapes) of individual lines, without performing the conventional spectral fit.

Plasmas are in non-equilibrium ionization (NEI) condition when  $T_e$  differs from  $T_z$ . NEI plasmas are observed from, for example, young supernova remnants, in which  $T_e$  is higher than  $T_z$  as described below. The parameter describing how closely the ionization degree reaches CIE is given by the product of electron density and elapsed time,  $n_e t$ . The actual value for a plasma to reach CIE is given by  $n_e t \sim 3 \times 10^{12} \text{ cm}^{-3} \text{ s}$ , in which  $t$  is measured from the onset of the gas heating caused by disturbing events (e.g., shock passage or gas collision) Masai (1984), Smith and Hughes (2010).

The most typical example of the NEI case is “ionizing plasmas”, where  $T_z$  is lower than  $T_e$  and the plasma is halfway through the ionization Masai (1984). This type of plasma is observed when a near-neutral gas cloud is shock heated, like in young supernova remnants. Electrons near the shock front are heated quickly, whereas heavy elements which are initially neutral will be gradually ionized by collisions with electrons until the above CIE condition is reached. Because ions are under-ionized in ionizing plasmas, inner-shell excitation through the electron impact and subsequent emission of fluorescent X-rays become important as an elementary process. The ratio of Fe K $\beta$ /K $\alpha$  line intensities is often used to diagnose how far the ionization and excitation are advanced, because K shell transitions give relatively high fluorescent yield and the two emission lines are well separated in energy.

Another NEI case is “recombining plasmas” with  $T_e < T_z$ , opposite to the ionizing plasmas. Observationally,  $T_e$  determined from the continuum spectrum is lower than  $T_z$  which can be estimated from emission lines and recombination edges. In fact, strong radiative recombination continuum, an edge-like feature in the spectrum, has been recognized from some type of supernova remnants Yamaguchi et al. (2009), Ozawa et al. (2009). The question is how electrons underwent significant cooling even after causing ionization of all the heavy elements. It has been proposed that a shock break-out scenario can explain the observed NEI feature. In an early phase of the evolution of the supernova remnant, when the shock passed through a dense gas, the plasma was heated and highly ionized through shock heating. Then, after the shock breakout, a low  $T_e$  was produced due to rapid cooling caused by an adiabatic expansion. During this expansion,  $T_z$  takes much longer time to cool down.

In contrast to the collisional plasmas, photoionized (PIE) plasmas are exposed to strong external radiation, and the radiative ionization balances with radiative and dielectronic recombination (e.g., Kallman et al. (2004)). Since collisions are not efficient, electron temperature  $T_e$  is usually much lower than the ionization temperature  $T_z$ , and the plasma can be in ionization conditions which are much different from those of collisional plasmas. This type of plasma is observed in e.g., broad line regions of active galactic nuclei (AGN) or a gas surrounding bright compact objects. Actual ionization condition depends on the intensity and hardness of the incident radiation spectrum, on the distance of the matter from the radiation source, and also

on the density and geometry of the matter. Therefore, modeling of the PIE plasma is usually complicated and one has to make simplified geometrical assumption of the system. The ionization states of the PIE plasma can be broadly estimated by the ionization parameter  $\xi \equiv L/nr^2$ , with the ionizing luminosity  $L$ , gas density  $n$ , and distance from the ionizing source  $r$ , respectively.

## 2.4 He-like ions

He-like ions of elements from O to Ni show high abundance over a wide range of temperature as depicted in Fig. 3 due to their stable electronic configuration, and their emission or absorption lines are strong for many cosmic X-ray sources. The ions have a simple structure, with only two electrons, showing a few characteristic atomic transitions which are well understood. They are very useful in examining the plasma properties, such as density, temperature, and geometry without fitting with spectral models. Since high resolution X-ray spectroscopy can resolve the line features in detail, we describe here the characteristics of transitions in some detail. A detailed account of the properties of He-like ions is given by a review paper Porquet et al. (2010). In  $n = 2$  to  $n = 1$  transitions, with  $n$  the principal quantum number, there are four strong emission lines, namely resonance ( $w$ ), forbidden ( $z$ ), and two intercombination lines ( $x$  and  $y$ ). Figure 4 shows a schematic diagram of the energy levels of He-like ions. The resonance line  $w$  is emitted in the allowed transition, and

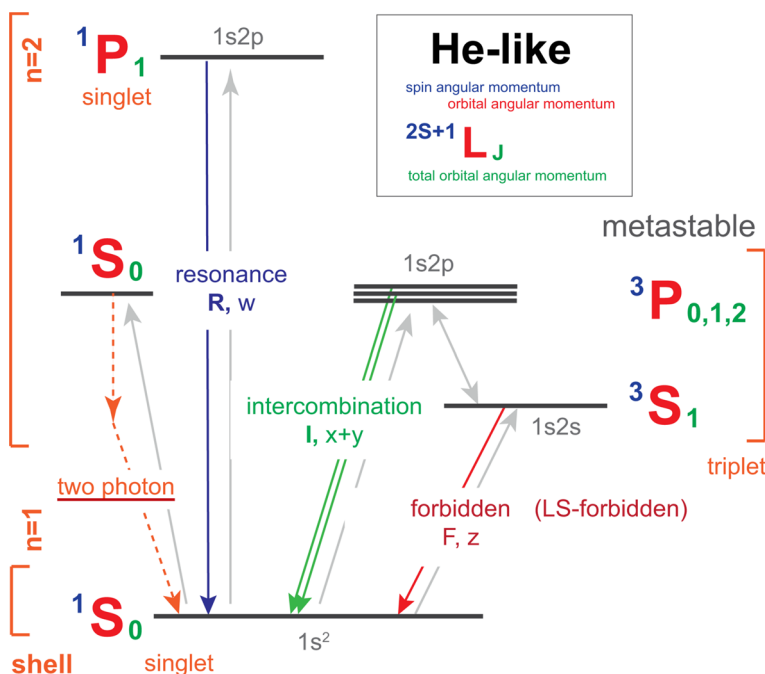


**Fig. 4** Schematic diagram of energy levels in He-like ions ASTRO-H CookBook Members (2015)

these line photons can be absorbed and re-emitted (called as resonance scattering) if the plasma is optically thick only to the resonance transition. Intercombination lines ( $x$  and  $y$ ) are emitted from the upper triplet levels to the singlet ground state. Forbidden line  $z$  is emitted only when the plasma density is very low as described below. Line splittings of these  $w$ ,  $x$ ,  $y$  and  $z$  lines are on the order of several to 20 eV for He-like C ( $Z = 6$ ) to Fe ( $Z = 26$ ) ions, which correspond to ~1 to 2 % differences in energies relative to the average centroid of the line complex.

Line width, for both emission and absorption, has the following origins, except for that due to the detector resolution; (i) natural width, (ii) thermal Doppler motion, and (iii) turbulence. The natural width, with a Lorentzian shape, reflects the uncertainty principle, and it is inversely proportional to the life time of the upper level. It is pointed out that X-ray transitions take much shorter time than optical transitions, and the natural width of allowed transition, such as  $w$  from He-like Fe ion, can be an order of eV Watanabe (1975). The thermal Doppler broadening is Gaussian shape, and its width (Gaussian sigma) is given by

$$\sqrt{\frac{2kT_i}{m_i c^2}} E_0$$

where  $E_0$  is the original line energy,  $T_i$  is the ion temperature, and  $m_i$  is the mass of ion. It is about 2 eV for a Fe-K line, at  $E_0 \sim 6700$  eV, with  $T_i = 5$  keV. Finally, the turbulence width is also Gaussian and given by

$$\frac{v_{\text{turb}}}{c} E_0$$

in frequency where  $v_{\text{turb}}$  is the turbulent velocity. A velocity of 100 km s<sup>-1</sup> gives a width of about 2 eV for the Fe-K line. These considerations, in particular the possible limit by the natural line width, imply that ultimate energy resolution which can bring meaning plasma information could be a fraction of eV.

In a CIE plasma with low plasma density, with  $n_e \lesssim 10^{10}$  cm<sup>-3</sup>, electrons in the  $^3S_1$  state decay to the ground state ( $^1S_0$ ) by emitting the  $z$  line because  $\Delta L = 0$  for transitions involving a spin flip violates the selection rule. The low probability of collisions hampers electrons to make transition to other levels, and radiative transition by emitting a forbidden line to the ground state is the only way of de-excitation. In higher densities, collisions between electrons and ions allow electrons in this metastable level,  $^3S_1$ , to be collisionally excited to the  $^3P_{1,2}$  levels. This will be followed by an emission of  $x$  and  $y$  lines, which are not forbidden. Based on this, the ratio  $R = z/(x + y)$  is thus used as an indicator of the electron density.

Another ratio  $G = (x + y + z)/w$  is a good measure of the electron temperature. Excitation from the ground state to the  $^3S_1$  and  $^3P_{1,2}$  states involves spin exchange, and its probability has weaker temperature dependence than the excitation to the  $^1P_1$  level which requires no change of spin. The strong temperature dependence of the  $w$  line makes the  $G$  ratio a good indicator of the temperature. The actual temperature dependence of the  $G$  ratio in the CIE plasma is shown by solid curves in the bottom panel of Fig. 5 for different elements.

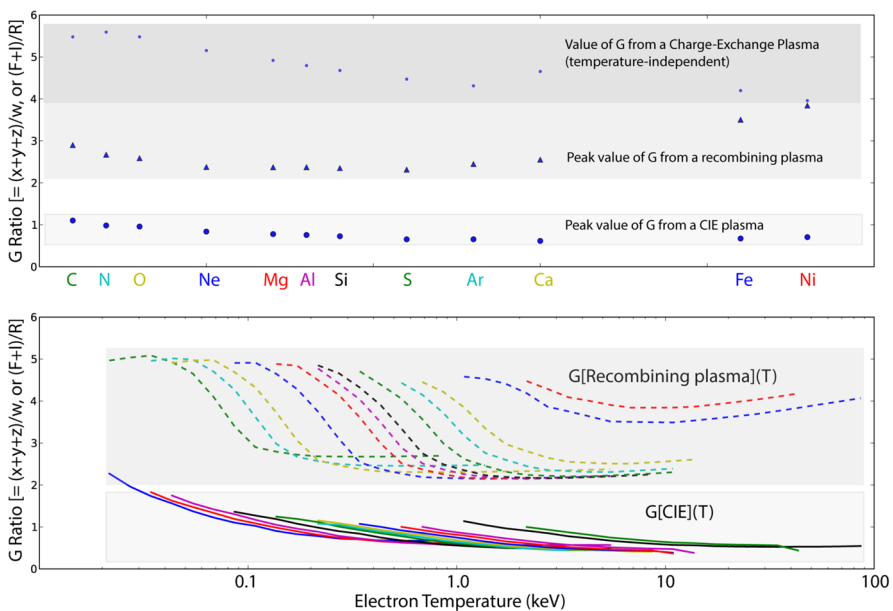


**Fig. 5** (Top) Comparison of peak He-like  $G$  ratio for charge-exchange plasma, recombining plasma, and CIE plasma. (Bottom)  $G$  ratio as a function of electron temperature in recombining and CIE plasmas. Taken from Smith et al. (2014)

In a recombining plasma, the levels are occupied according to their statistical weights, different from the CIE plasma which is governed by the Boltzmann factor. This gives higher weights to triplet levels and the  $G$  ratio becomes larger than the CIE plasma as displayed by dashed curves in the bottom panel of Fig. 5. At higher temperatures and with sufficient density, however, ions tend to be more excited by electron collisions, resulting in a lower  $G$  ratio Porquet et al. (2010).

## 2.5 Charge exchange emission

X-ray emission has been observed from solar system objects including Jupiter, Saturn, Mars, Earth, Mercury, and comets, whose gravitational potential energy is nowhere near those of compact objects and, therefore, X-rays are produced by an entirely different mechanism. The X-ray emission from these objects is caused by incidence of solar X-rays and solar cosmic-rays interacting with the solar system objects. Also, relatively strong electromagnetic fields are involved in the case of Jupiter and Earth.

Charge exchange is a process which give rise to X-ray emission and has been recognized in 1990s to operate in the solar system objects Dennerl (2010). This is a reaction in which hot plasmas or ionized cosmic rays come into contact with cold gas. The strong Coulomb force of ions strips an electron(s) from the neutral atom or molecule in the cold gas. Then, the electron enters into an excited state of the

ion and cascades to the ground state by emitting X-ray and UV lines. Therefore, the emitted spectrum consists exclusively of emission lines. With the charge exchange process, we can examine gas properties in the boundary region where ionized and neutral matter encounter each other. This process is characterized by a large cross section, on the order of  $10^{-16}\text{cm}^2$ , and can probe matter with very low density such as gas evaporating from planetary and cometary surface.

Because of the large cross section, the charge exchange is characterized by high line intensities in low density environments. Transitions from high principal quantum numbers ( $n \gtrsim 3$ ) to the ground state are often stronger than those in CIE plasmas because the dominant electron capture level in the collision of a highly stripped ion with neutrals can be a state with such a high principal quantum number. The  $G$  ratio, described above, can also be used to examine if the charge exchange process works in the system. Since the excited states for the  $z$  and  $x + y$  lines have larger multiplicity than for the  $w$  line,  $G$  ratio is systematically large in the charge exchange emission. This is shown in the top panel of Fig. 5.

Since the charge exchange processes should work whenever hot plasmas or ionized particles interact with cold matter, the characteristic line features (strong  $z$  from He-like ions and transitions from high  $n$  states) will be detected from many objects outside the solar system (e.g., clusters of galaxies and supernova remnants) with improved energy resolution.

In Fig. 6, we show an SXS simulation of solar wind charge exchange emission. Compared to the CIE plasma model, the charge exchange emission is characterized by strong  $z$  from OVII ion, as described before. The emission is produced by solar wind interacting with the earth's atmosphere and its spatial distribution would tell us

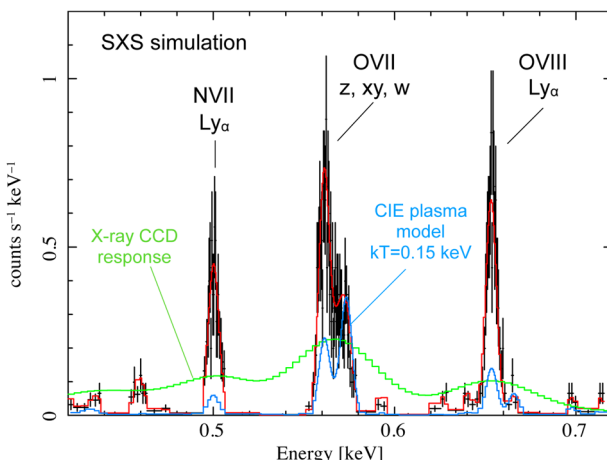


**Fig. 6** SXS simulation of solar wind charge exchange emission in Earth's exosphere based on a Suzaku observation during a strong geomagnetic storm Ezoe et al. (2011). The assumed exposure time is 50 ks. Red and green solid lines indicate the best-fit Gaussian models and the spectrum when observed with an X-ray CCD, respectively. For comparison, a CIE plasma model assuming  $kT = 0.15$  keV and a solar abundance is plotted in blue. The CIE model is normalized to have the same line intensity as that from the charge exchange model at  $w$  from OVII ion for clarity

how solar wind enters into the magnetosphere and exosphere of Earth. The charge exchange emission is extended over the field of view of the instrument, because of the spatial size and proximity of the emitting region. If mapping observations are performed, it would be a unique way to visualize the structure of the Earth's magnetosphere (e.g., Branduardi-Raymont et al. (2012), Sibeck et al. (2018), Ezoe et al. (2018)).

## 2.6 Absorption and reflection

X-rays are subject to absorption and/or reflection when there exists matter either intervening the line of sight or located in the neighborhood of the emitting source. These processes enable us to study the properties of the matter, even when the matter itself does not emit detectable emission due to low temperatures typically. The intervening matter causes continuum absorption and line absorption in the X-ray spectrum. The continuum absorption in the X-ray band is dominated by photoelectric effect, and the absorbed spectrum is characterized by absorption edges with saw-tooth structures. The energy and depth of absorption edges tell us the absorbing species, ionization state and column density, enabling us to infer geometrical information such as the distance of the absorber from the source, gas density and line-of-sight depth.

Let us now look into the absorption lines for which the high resolution spectroscopy is a powerful tool. Typical absorption lines in X-rays are generated through upward transitions of electrons in the outermost atomic shells to a level with different principal quantum number. Strong absorption lines correspond to normal resonance lines. The center energy of the absorption line tells the line-of-sight velocity of the absorber. For example, blue-shifted absorption lines from warm material have been observed from AGNs. Outflow velocities range from a few hundred to a few thousand  $\text{km s}^{-1}$ . There is a tight relation between the mass of supermassive black holes and the bulge mass of host galaxies, and such fast outflows may be connected to the feedback process which controls the co-evolution of the black hole and galaxy Kormendy and Richstone (1995) as depicted later in Sect. 3.3.

Equivalent width of the absorption lines does not vary strongly with the nuclear charge, in contrast to the emission lines, and oxygen, the most abundant element, shows the strongest absorption lines Kaastra et al. (2008). The line strength is proportional to the oscillator strength, which is large for the reverse transition of  $w$  line shown in Fig. 4.

We also touch upon the reflection process. The word “reflection” is used for the process where incident X-rays are scattered outward at the surface of relatively cool material, such as accretion disks, around X-ray bright black holes or compact stars, and stellar surfaces. The basic processes are Thomson and Compton scatterings along with fluorescent line emission. When the incident spectrum has a power-law form with a photon index of about 2 extending up to  $\gtrsim 100 \text{ keV}$ , the reflected spectrum, such as one from an accretion disk, shows a broad peak at 20 keV. At this energy, Compton scattering is dominant over both photoelectric absorption (strong at lower energies) and Compton recoil losses (at higher energies). Fluorescent

emission lines from low ionized atoms in the reflecting matter also help us estimate the physical properties and geometry of the matter.

Sensitivity to the absorption lines and reflection spectra depends on the intensity of the continuum source and the energy resolution of the detector, as well as the intrinsic strength of the absorption and reflection features. The signal to noise ratio for the detection of absorption line is given by,

$$\text{S/N} = \sqrt{A(E) t F(E)} \frac{W}{\sqrt{\max(\Delta E, W)}},$$

where  $E$  is energy,  $A$  is effective area,  $F$  is photon flux per unit area, time and energy,  $W$  is equivalent width of the line, and “max” is the greater of the two, respectively Kaastra et al. (2014).

A better energy resolution enables higher sensitivity, as long as the intrinsic line width is narrower than the energy resolution. Fig. 7 shows a simulated spectrum of NGC 4151, a bright AGN, based on the parameters of a previous *Chandra* observation. There are prominent absorption lines at 1.8 and 2.2 keV, clear signatures of highly ionized Si and S which are photoionized by the central source. Similar to the emission line diagnostics, the line width and the line center energy tell us the ionization state of the surrounding matter and the velocity of the outflow. If time variation of the absorbed or reflected component shows a systematic delay to the central continuum, the distance of the gas from the central AGN can be estimated.

### 3 X-ray study of astrophysical plasmas

#### 3.1 Advantage of X-ray observations

Since the first rocket experiment in 1962, X-rays have been detected from various astrophysical objects in the Universe, namely from near-by solar system objects to distant clusters of galaxies and supermassive black holes. Such a ubiquity of X-ray

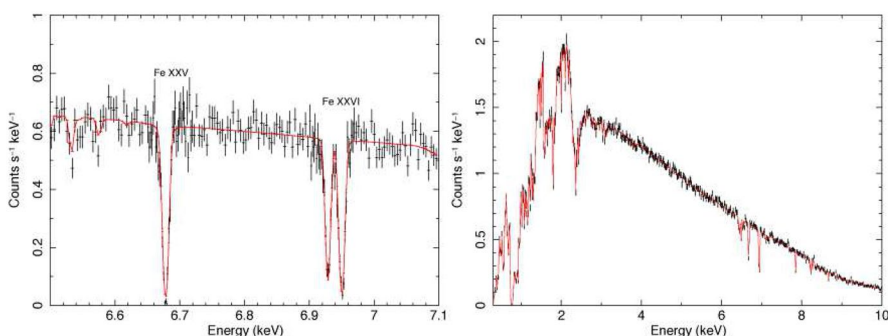


**Fig. 7** SXS simulation of NGC 4151 for 100 ks exposure Kaastra et al. (2014). Red lines indicate assumed model curves

emission was totally unexpected before the beginning of the X-ray astronomy, and the X-ray astronomy has played a major role in changing our concept of the Universe from a static and quiet one to a dynamically evolving one. The detection of X-ray emission has shown that energetic processes, involving gas heating and particle acceleration, do operate much more commonly in many categories of astrophysical systems. X-ray observations of plasmas have provided us with valuable information regarding their physical properties and environments, leading to an improved understanding of the Universe.

Among the wide wavelength range of electromagnetic waves, X-rays are particularly useful in studying the properties of astrophysical plasmas. In the X-ray energy range of 0.1 keV to a few times 10 keV, almost all the emission and absorption lines are produced via atomic transitions involving a change of principal quantum number. Therefore, important atomic processes (not simply limited to ionization and excitation) give spectral signatures in the X-ray band. As the energy resolution of instruments is improved, our knowledge on the plasma properties has become deeper and deeper.

### 3.2 Clusters of galaxies

To show how X-ray spectral study gives fundamental information on plasmas, we here look at clusters of galaxies as the first example. These systems comprise hundreds to thousands of galaxies, with the intergalactic space filled with X-ray emitting plasmas Sarazin (1986), Böhringer and Werner (2010). These are the largest gravitationally relaxed structures in the Universe. Clusters have the radius of typically 3 Mpc (10 million light years), and their formation takes cosmological time of more than 10 billion years and the gravitational contraction is still in progress. Observations indicate that the gravitational mass of clusters can be broken down to galaxies (5%), hot plasma (20%) and dark matter (75%), and the mass fractions are about the

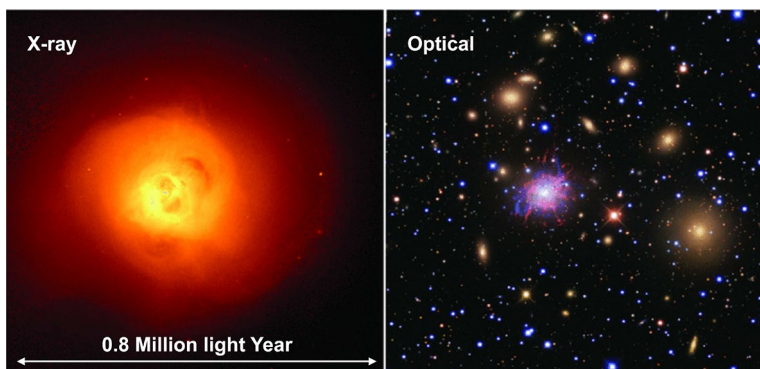


**Fig. 8** X-ray and optical images of the Perseus cluster Fabian et al. (2011), Gabany (2009). Stars and galaxies are shown in the optical image, whereas the X-ray image provides a huge amount of plasma distributed across a wide region

same in most of X-ray bright clusters. As shown in Fig. 8, the X-ray image clearly shows that the space between galaxies is filled with hot and low-density plasma.

Plasmas in clusters are heated by slow gravitational contraction, and the hot plasma is approximately under hydrostatic equilibrium in the gravitation potential of dark matter. In this case, the pressure gradient of the hot plasma is balanced against the gravitational pull as,

$$\frac{1}{\rho_{\text{gas}}} \frac{dp}{dr} = -\frac{GM(r)}{r^2}$$

with pressure  $p$ , gas mass density  $\rho_{\text{gas}}$ , and gravitational mass  $M(r)$  within a radius  $r$ . Measurement of the plasma density and temperature as a function of radius in the cluster space will enable us to estimate the distribution of gravitational mass, which is dominated by dark matter. Even though clusters become X-ray faint as one goes to outer region, high sensitivity of X-ray satellites, such as Suzaku, can probe near the virial radius of clusters, namely the outer boundary of the virialized portion of the cluster system. The X-ray observations of clusters of galaxies have thus shown fairly detailed spatial distribution of dark matter. Cosmological evolution of mass function of clusters gives strong constraint on the cosmological parameters including the fraction of dark energy. Also, the observed ratio of dark matter to baryon masses is almost constant among clusters and this constrains the total matter density  $\Omega_m$  of our Universe. In this way, clusters of galaxies play a key role in the observational cosmology.

X-ray spectroscopy shows that hot plasmas contain heavy elements, from O to Ni, with a typical abundance of 0.3 times solar. This simply indicates that galaxies have expelled large amount of metal-rich gas to the intergalactic space. The distribution and relative abundance of these elements enable us to study how and when galaxies produced metals in the evolution history of the Universe. Here, the deep gravitational potential of clusters help preserve all the heavy elements produced in the past, contrary to that galaxies have lost them through galactic winds or ram-pressure strippings. In this view, X-ray spectra of clusters of galaxies contain rich information in tracing the chemical history of the Universe, probably going back to the time of galaxy formation. Figure 9 shows an X-ray spectrum, taken by CCD instrument with continuum component subtracted, emitted from a central region of a cluster of galaxies. Numerous emission lines from oxygen to iron are detected, confirming that a large amount of metals have been created by the past star formation activities in the constituent galaxies. Their detailed distribution would tell us the metal injection mechanism, such as either by galactic winds or by ram pressure stripping. Spatial distribution of temperature, density, and heavy elements of the plasma can be obtained from such spatially resolved X-ray spectra. Theoretical models of X-ray emission from plasmas have been refined by comparing with the observed X-ray spectra, and these models are useful in obtaining the plasma parameters and in estimating how much ambiguities they have.

Furthermore, observations of the cosmic microwave background (CMB) and the Big Bang nucleosynthesis studies have put tight constraints on the abundance of baryons in the Universe. The Big Bang nucleosynthesis predicts the abundance

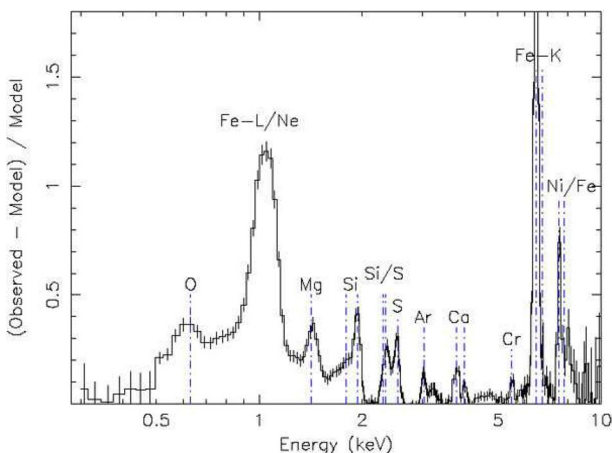


**Fig. 9** X-ray spectrum of the cluster 2A0335+096 obtained with XMM-Newton Werner et al. (2006). The vertical axis is obtained by fitting the spectrum with a model without lines and subtracting the best-fit model from the data to clarify emission lines from various elements

of baryons which precisely coincides with the CMB observations. However, more than half of baryons in the local Universe are undetected. This discrepancy is known as the missing baryon problem. Cosmological hydrodynamical simulations predict that they are believed to exist as X-ray emitting plasmas, with  $T \gtrsim 10^6$  K, associated with large scale structures of the Universe Fukugita and Peebles (2004), Read and Trentham (2005). The missing baryons are diffuse and hence difficult to detect so far. Hence, X-ray observations can probe hot and dominant part of baryons in the Universe, and we will know their whereabouts along with their temperature, density and metallicity. This is not possible with other wavelengths.

### 3.3 Stellar and collapsed objects

Here, we look into other types of X-ray objects for which the high resolution X-ray spectroscopy again gives crucial information about the physics going on in extreme environments. As mentioned before, X-rays are produced in a region which has strong gravity, intense magnetic field, and high gas motions, for which X-rays would be the only means of directly probing the exotic physical conditions (see e.g., Giacconi and Gursky (1974), Oda (1984), Longair (1994), Mannings et al. (2000)). A more detailed review is available in e.g., Kaastra et al. (2008).

More than a thousand X-ray emitting young stars were discovered in the Orion nebula Getman et al. (2005). Most of the X-ray bright sources are low-mass stars, like the Sun, which exhibit strong X-ray activity as indicated by high ratio of the X-ray to the bolometric luminosities. This is because the plasmas are heated in violent magnetic reconnection flares, connected with active convection within the stars. X-ray observations of the Sun indicate that magnetic reconnection events accelerate particles up to MeV, causing intense hard X-ray emission. In this way, X-ray measurements give a unique diagnosis of magnetic activity of young stars.

Massive stars ( $> 10 M_{\odot}$ ) also emit X-rays but, with smaller outward temperature gradient near the surface, they lack the strong convection zone unlike low-mass stars. The X-ray emission mechanism of these massive stars are therefore considered to be different from those of low mass stars and still under debate. The most favored model is that X-ray emission arise from shocks due to fast and massive stellar winds with a typical velocity of  $2000 \text{ km s}^{-1}$  and a mass loss rate of  $10^{-6} M_{\odot} \text{ yr}^{-1}$ , which are  $\times \sim 4$  faster and  $\times \sim 10^8$  heavier than those of the Sun, respectively Güdel and Nazé (2009). The massive stars profoundly affect their surrounding medium by their strong ionizing radiation and large mechanical energy in a host galaxy. X-ray observations can probe their high energy activity at work.

Strong X-ray sources detected from the early days of X-ray astronomy are close binary systems consisting of a compact star (neutron star, white dwarf, or black hole) and a normal star Longair (1994). There are hundreds of such sources in our Galaxy, and, even they are point-like, their time variation helped us clarify the detailed properties of the systems. In most cases, gas of ordinary star accretes to the compact star which has a compact gravitational equipotential surface with strong gravity. From X-ray studies, structure of accretion disks, its instability, funneled gas flow onto magnetized compact stars, and outflow from the disk have been understood down to a surprising detail. Even physics of the compact stars themselves (e.g., the interior of the neutron star) have been advanced with fast timing studies.

As for a galaxy scale activity, supermassive black holes in the centers of galaxies still provide us with many puzzles and problems. Their X-ray luminosity goes up to around  $10^{45} \text{ erg s}^{-1}$ , making them the brightest objects along with clusters of galaxies in the X-ray sky. Time variability over a month or shorter, as well as the presence of cosmic jets, clearly indicates these central objects to be black holes, since no other objects in the Universe can exhibit such an immense activity. Interestingly, the estimated mass of the central black hole is proportional to the bulge mass of the host galaxy over 4 orders of magnitudes in the galaxy mass. The black hole mass is typically 1/1000 of the bulge mass, and it is not clear how black holes and galaxies can coordinate in their mass-growing evolution. It is discussed that a certain feedback mechanism is in operation between the two, but we do not have a direct evidence for such a process. Possibly, outflows from the black hole system may affect and control the galaxy evolution. High-resolution spectroscopy would show us the gas dynamics (velocity, outflow mass) directly as shown in Fig. 7 and it is hoped that X-ray studies of these feedbacks would give us a clue to solve this co-evolution mystery in near future.

As mentioned before, not only exotic astronomical objects, as described here, but also other general objects, including solar system objects, emit X-rays. X-ray study has thus taught us “the inexhaustible wealth of nature, a wealth that goes far beyond the imagination of man” as stated by Bruno Rossi, who pioneered the X-ray astronomy Clark (1998). His colleagues include a Nobel laureate Riccardo Giacconi and a Japanese researcher Minoru Oda, who was a distinguished leader of Japanese space astronomy.

### 3.4 History of X-ray spectroscopy in astrophysics

X-rays below  $\sim$ 20 keV, which are generally abundant in photon flux, are photoabsorbed in the atmosphere. Even those with higher energies are Compton scattered. Therefore, it is essential, using rockets, balloons, or satellites, to take the instrument above the atmosphere to an altitude of more than 150 km. The first observation of astronomical objects other than the Sun was performed in 1962 with a rocket experiment by a group at American Science and Engineering. The experiment intended to investigate the solar X-rays scattered on the surface of the Moon. Although the X-ray flux from the Moon was far below the sensitivity at that time, the diffuse X-ray background and a very bright X-ray source, Scorpius X-1 which is considered to be a neutron star with matter accretion from a companion star, were detected Giacconi et al. (1962). To date, millions of X-ray emitting objects have been detected, in particular with all-sky survey observations. About thirty X-ray astronomy satellites have been launched, and their sensitivity, characterized by the effective area and the angular and energy resolution, have been greatly advanced. The United States, Russia, Japan, and European countries have launched most of the satellites so far, whereas India (Astrosat) and China (HXMT) joined the group with their first X-ray astronomy satellites in the late 2010s. The chronology of X-ray astronomy satellite is shown in Fig. 10. The history of X-ray astronomy has been summarized in previous articles, e.g., Bradt et al. (1992), Giacconi (2009). Recent satellites launched after 2010s and those scheduled for launch are described in homepages of space agencies [39], ESA Science and Technology (2019), JAXA (2019), China National Space Administration (2019), [43]. Observed data are mostly archived and are freely available from the agency pages. In total, we have approximately ten X-ray

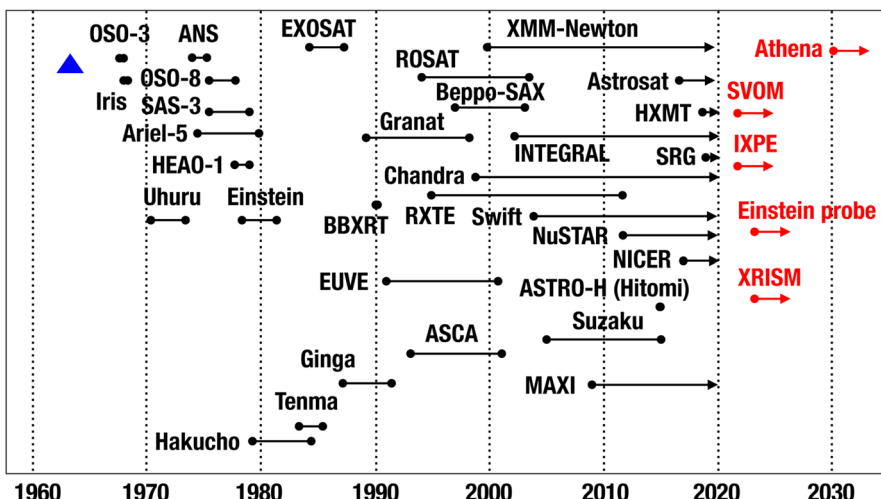


**Fig. 10** History of X-ray astronomy satellites. Arrows indicate that the satellites continue observations. Two future missions (XRISM and Athena) are also plotted. The triangle indicates the X-ray rocket experiment in 1962 in which Scorpius X-1 was discovered

astronomy satellites including the payloads onboard the International Space Station currently in operation.

Here, we briefly review the history of X-ray astronomy, focusing on the improvement of energy resolution, shown as FWHM energy resolution at 6 keV. During the past 60 years, the spectroscopic capability, regarding the energy resolution and measurable energy range, has been advanced by orders of magnitude. Such a fast improvement was made possible by the basic technology advancements in these years, as well as by the frequent launch of new missions. Other capabilities, such as the effective area, field of view, angular resolution, time resolution, ability/inability of observing extended sources, and hardware complexity have also showed great progress over the years, and pushed X-ray astronomy to play a substantial role in astronomy and astrophysics. The improvement history of energy resolution of X-ray instruments and major findings, which resulted from the spectral study, are summarized in Fig. 11.

Proportional counters were the first detectors widely used in the beginning of X-ray astronomy before  $\sim$  1980, with an energy resolution of about 20% FWHM at 6 keV, equals to 1200 eV. These are gas counters and the electron multiplication in the gas causes large fluctuation of the output signal. Despite the limited energy resolution, Fe-K lines from bright X-ray sources such as clusters of galaxies, AGNs, and galactic sources were detectable.

The energy resolution was improved by a factor of 2–3 by gas scintillation proportional counters, in which UV light emitted by photoelectrons during their drift through the detector gas was measured. The conversion to the UV light without causing an electron avalanche provides a signal amplification with relatively small

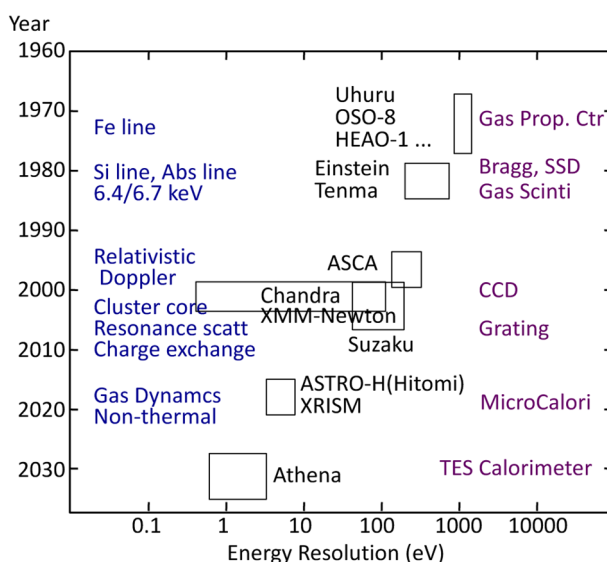


**Fig. 11** History of energy resolution of X-ray spectrometers in X-ray astronomy. The energy resolution is FWHM in energy for 6 keV X-rays. The rectangular box for Chandra and XMM-Newton represents performance for gratings for point sources. Revised from the original figure in Bradt et al. (1992)

fluctuation. With this resolution, the fluorescent Fe K-line at 6.4 keV and the thermal H-like or He-like Fe line at 6.9/6.7 keV are clearly separated. Ionization conditions and temperatures of the plasmas were investigated from the ratios of the H-like and He-like lines directly without fitting with complicated spectral models but with simple models composed of Gaussian(s) plus a continuum. Further, with the wide field of view (nearly 50 arcmin in diameter) of the gas imaging spectrometer on ASCA, launched in 1993, strong concentration of iron in the centers of several clusters of galaxies has been detected. Also, the imaging spectroscopy data showed absence of cool gas in the core of clusters of galaxies Fukazawa et al. (1994), Makishima et al. (2001), suggesting that extra heat input by AGN jets or by other mechanisms may be counteracting the strong radiative cooling.

Solid-state spectrometer onboard the Einstein observatory gave an energy resolution of about 150 eV in 0.4–4 keV with no imaging capability, and it suffered from ice accumulated on the detector surface due to the low operational temperature of ~100 K. X-ray CCDs, whose first application in X-ray satellites was also on ASCA, improved the energy resolution to 100–150 eV by about an order of magnitude over the proportional counters. Thus, study of elemental abundances in clusters of galaxies and supernova remnants have advanced dramatically. An indication of broadening of the Fe K-line from AGN, caused by a combined effect of special and general relativity on the reflecting gas in the inner region of accretion disk, was also discovered Tanaka et al. (1995).

Dispersive techniques have been developed. The Bragg crystal spectrometer was used on Einstein, followed by diffraction gratings onboard the Chandra and XMM-Newton both launched in 1999. In the dispersive technique, in contrast to the non-dispersive technique for the photon detection, the wavelength of X-rays is measured by dispersion angles. The energy resolution depends on the density of grooves as well as on the angular resolution of the optics. The advantage of dispersive method lies in the good wavelength or energy resolution for point sources, as compared with the CCD resolution, especially for soft X-rays below ~2 keV. In fact, the wavelength resolution becomes better for softer X-rays, contrary to the photon detecting instrument. The drawbacks are a partial loss of the effective area due to the grating efficiency and degradation of the energy resolution for extended objects since gratings basically work on a strictly parallel incident beam.

For example, emission lines from hot stellar corona and absorption lines in AGNs were studied in great detail with the gratings. The resolving power ( $E/\Delta E$ , with  $\Delta E$  indicating an approximate FWHM) is 500–1000 at 1 keV. The energy resolution is degraded for extended X-ray sources like clusters of galaxies and supernova remnants. However, the grating observations from XMM-Newton brought a clear evidence for the lack of cool gas in the core of galaxy clusters Sanders et al. (2010), which confirms the ASCA results obtained with the gas scintillation proportional counters. Strong indication of charge exchange X-rays produced through interaction between hot plasma and cold gas clouds in a supernova remnant Katsuda et al. (2012) was likewise discovered.

Evidently, the energy resolution has played a key role, together with the angular resolution, in the historical development of the X-ray astronomy. Along this line, X-ray microcalorimeters, first proposed in the 1980s Mosley et al. (1984), were truly

revolutionary. The concept is rather simple; a tiny heat pulse generated by absorption of a single X-ray photon in the detector is measured by a highly sensitive thermometer. The energy resolution is limited by the fluctuations of phonon signal and noise in the thermometer. Individual phonons have a typical energy of  $kT$ , which is an order of  $\mu\text{ eV}$  at 50 mK, much lower than the energy, 3.6 eV, to produce electron-hole pairs in Si. With a much lower energy than typical carriers in semiconductors on the order of a few eV, phonons are produced in a far greater number. This gives a very small fluctuation of the signal determined by the total number of phonons. When operated in a very low and stable temperature environment (50–100 mK), a superb energy resolution of about 5 eV is achieved with microcalorimeters.

Although the concept of microcalorimeters is simple, in practice it has been a great challenge to develop a cooling system that can operate in the space environment. The system needs to provide a low and stable bath temperature for the detector, accomplished by employing either a cryogen, such as liquid He or solid Ne, or mechanical and magnetic coolers. The thermal and electrical environment need to provide the temperature stability on the order of 10  $\mu\text{K}$  or less. X-ray microcalorimeters were developed for X-ray astronomy satellites in the late 1980s and have been launched three times onboard ASTRO-E, Suzaku, and ASTRO-H. However, the first two failed to observe astronomical objects due to a rocket failure of ASTRO-E and a boil-off of the entire liquid helium in Suzaku, respectively. Finally, the X-ray microcalorimeter named the SXS (Soft X-ray Spectrometer) onboard ASTRO-H carried out the first astrophysical observations for about a month, as described in detail later.

## 4 ASTRO-H SXS

### 4.1 Overview

ASTRO-H is the sixth Japanese X-ray astronomy satellite, which was launched on February 17, 2016. It was the largest scientific satellite of Japan with a mass of 2.7 tons and a height of 1.7 m Takahashi et al. (2018). It was developed under a major collaboration between JAXA and NASA Goddard Space Flight Center (GSFC) with contributions from the European Space Agency (ESA), the Netherlands Institute for Space Research (SRON), the Canadian Space Agency (CSA) and Japanese, US, and European institutions. As for the observation instruments, ASTRO-H carried X-ray telescopes, X-ray CCDs, a soft gamma-ray detector, a hard X-ray imager, and the SXS. There are two distinctive features of the ASTRO-H satellite in comparison to the previous X-ray astronomy satellites. One is a capability of high-resolution spectroscopy with SXS covering an energy range 0.3–12 keV, and the other is the wide-band spectral coverage with high sensitivity, spanning a range from 0.3 to 600 keV with the suite of instruments.

The SXS has been developed by the long-lasting close collaboration between Japan and US institutes with participation from Europe Mitsuda et al. (2014). The collaboration has started in 1990s, at the time when the Japanese mission ASTRO-E (failed for launch in 2000) was designed to carry microcalorimeters onboard. Fig. 12 shows the SXS sensor chip and a schematic structure of each pixel. The

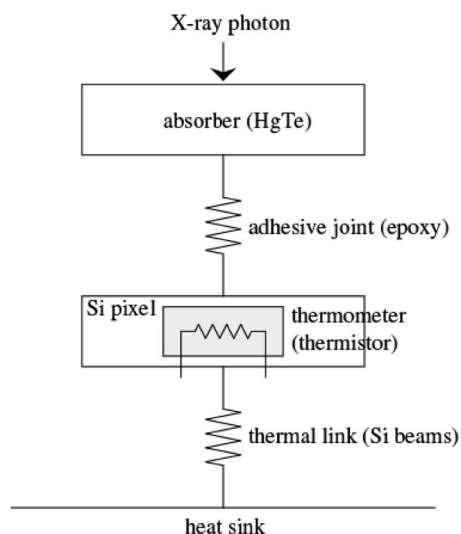
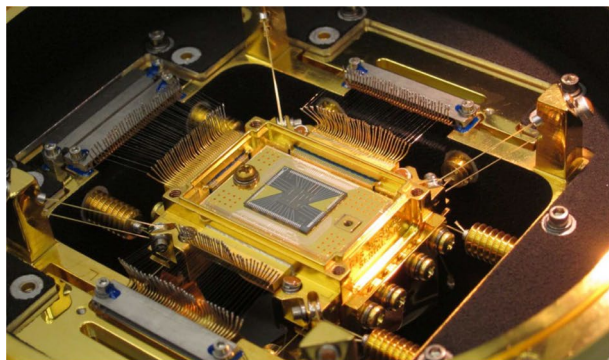


**Fig. 12** Photograph of SXS sensor and schematic structure of each pixel Eckart et al. (2018)

array format is a 5 mm square shape with  $6 \times 6$  pixels, covering  $3'.05 \times 3'.05$  of the sky. Each pixel is composed of a  $820 \mu\text{m}$  wide and  $10 \mu\text{m}$  thick HgTe absorber thermally connected to a doped silicon semiconductor thermistor. The energy range is 0.3–12 keV and the energy resolution at 5.9 keV is  $\sim 5$  eV in orbit. The pixel size and the absorber thickness are chosen to provide the necessary field of view and energy coverage. A larger heat capacity,  $C$ , tends to degrade the energy resolution as  $\Delta E \propto C^{1/2}$ .

Figure 13 shows the schematics of the SXS Dewar and its cooling chain. The sensor chip is cooled down to 50 mK with a three-stage adiabatic demagnetization refrigerator (ADR), 30 l of superfluid liquid helium (LHe), one Joule–Thomson (JT) cooler, and four two-stage Stirling (ST) coolers Fujimoto et al. (2017). The nominal lifetime requirement was three years, while the minimum and extra

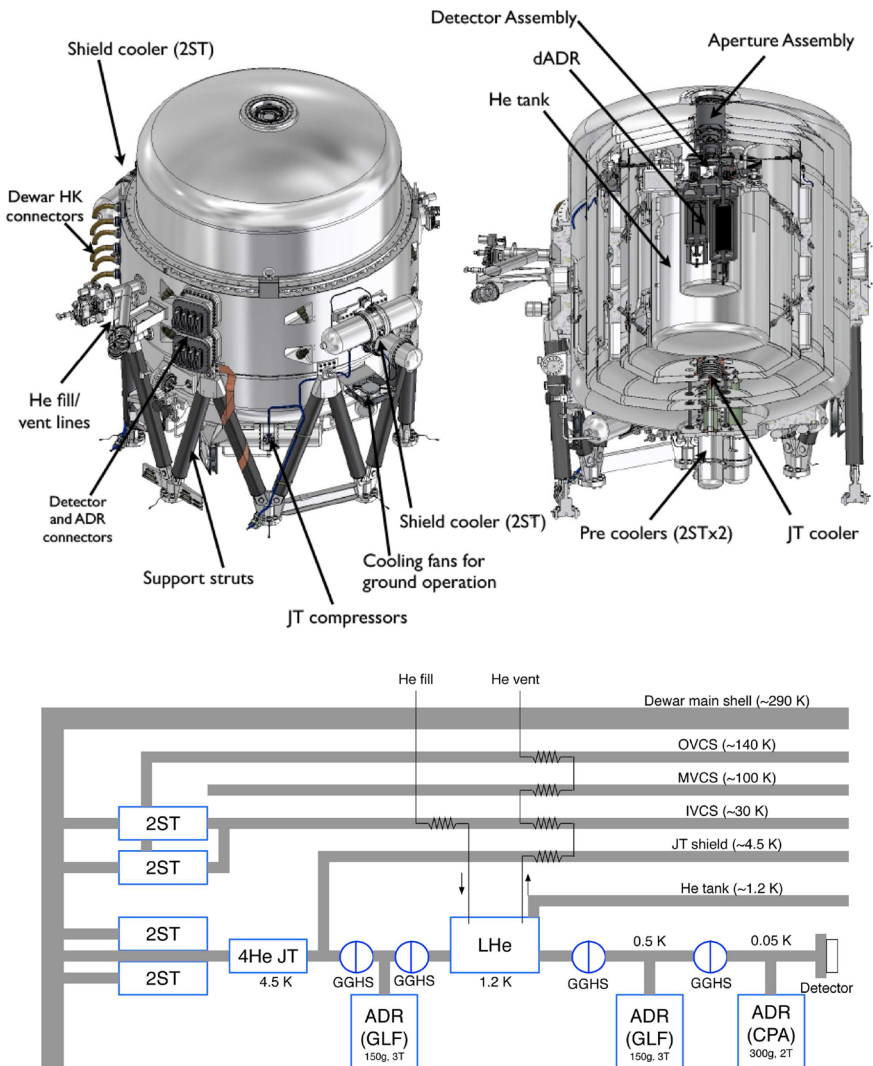


**Fig. 13** Schematics of SXS Dewar and its cooling chain Mitsuda et al. (2010). In the bottom panel, OVCS, MVCS, and IVCS denote outer, medium, and inner vacuum shields. GLF and CPA denote gadolinium lithium fluoride and potassium chrome alum, which are materials of the ADR salt pill. Grey lines and circles indicate shields inside the Dewar and heat switches for the ADR operation, respectively

success requirements were nine months and five years, respectively. Even after the LHe is exhausted, the cryocoolers can still keep the temperature low and the observation with the SXS can continue in principle. Because of this massive cooling system, the total mass of the SXS including electronics boxes and harnesses reached 425 kg. The average power consumption was 570 W, and most of it was consumed by the operation of the cryocoolers.

## 4.2 Comparison with past X-ray detectors

In Fig. 14, we plot the resolving power  $E/\Delta E$  of representative X-ray detectors including the SXS as a function of energy where  $\Delta E$  is energy resolution in FWHM at a certain energy  $E$ . The plot also shows resolvable spectral features of cosmic plasmas with black solid lines. This figure shows the state-of-the-art resolution achieved through the development history as illustrated in Fig. 11. The resolving power of different techniques depends on energy in different ways. Constant noise yields  $E/\Delta E$  proportional to  $E$ , while the fluctuation of signal carrier number yields an  $E/\Delta E$  proportional to  $E^{1/2}$ . Constant wavelength resolution  $\Delta\lambda$  yields  $\Delta E \propto E^2$  since  $E \propto \lambda^{-1}$ , and hence  $E/\Delta E$  is proportional to  $E^{-1}$ .

The typical resolving power of an X-ray CCD increases with energy, because its energy resolution depends on both the read-out noise and the Poisson fluctuation of the number of electron-hole pairs. At low energies below 1 keV, the energy resolution is approximately 50 eV, dominated by the read-out noise. In contrast, around 6 keV, the energy resolution is approximately 100 eV, and it is more dominated by the statistical fluctuation of the number of electron-hole pairs into which the incident X-ray energy is converted.

Gratings enable high-resolution spectroscopy for point sources. All the curves for gratings onboard the Chandra and XMM-Newton satellites decrease with energy, because the gratings have a constant wavelength resolution. LETG and MEG give the energy resolution comparable to CCD in the energy range 5–10 keV.

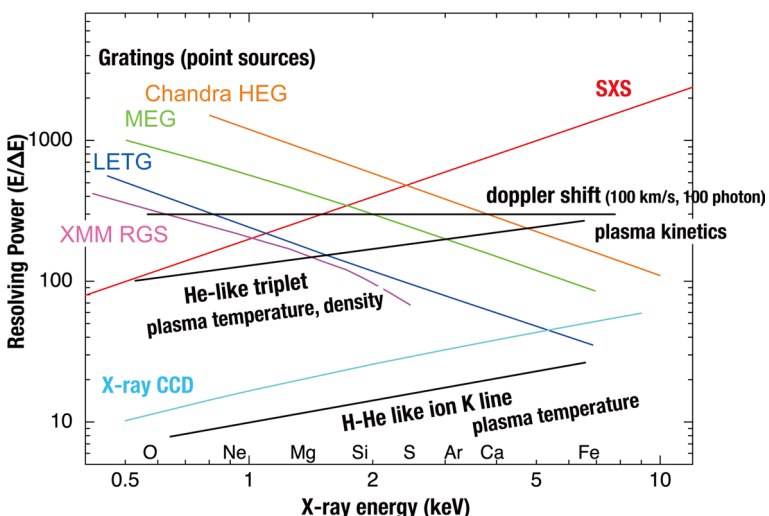


**Fig. 14** Resolving power of various X-ray detectors as a function of X-ray energy. Revised from the original figure in Mitsuda et al. (2010). Black lines indicate the resolving power required to distinguish K lines from H and He like ions, triplet lines from He-like ions, and a Doppler shift with  $100 \text{ km s}^{-1}$  accuracy. The red line represents the actual resolving power ( $\Delta E \sim 5 \text{ eV}$ ) of the SXS. Orange, green, blue, and magenta lines represent gratings onboard past X-ray astronomy satellites. The cyan line depicts a typical X-ray CCD performance

The gratings onboard the X-ray astronomy satellites are slit-less to maximize the signal flux. Consequently, the energy resolution decreases for extended X-ray sources or for point sources if nearby sources enter the field. Slit gratings (e.g., Kobayashi et al. (2018)) can avoid this disadvantage, but the field of view is severely limited. The X-ray microcalorimeters have a clear advantage over the gratings and provide integral field spectroscopy, i.e., a combination of spectroscopic and imaging capabilities, with superb energy resolution.

Similar to the X-ray CCD, the SXS has almost constant energy resolution as a function of energy. The in-orbit performance of the SXS is thus represented by a straight line ( $\propto E$ ) in Fig. 14. The SXS gives the highest resolving power above about 2 keV. Further, because the SXS is a non-dispersive detector, this resolving power is achieved even for extended X-ray sources.

The resolving power of the SXS enables distinction of emission lines not only for different ionization states, such as H- and He-like ions, but also for He-like triplet lines. Further, we can determine Doppler shifts due to plasma motions with an accuracy better than 100 km s<sup>-1</sup> as described later.

The increasing resolving power of the SXS as a function of energy facilitates the separation of line structures with better resolution for heavier elements. At the energy of the iron K line around 6 keV, the SXS exhibits high resolving power of  $E/\Delta E > 1000$ , which is important for the diagnosis of high temperature plasmas containing H and He-like iron ions in e.g., clusters of galaxies and supernova remnants, as well as cold matter exhibiting fluorescence lines from accretion disks around black holes.

Figure 15 shows the effective area of the SXS compared with those of the gratings. The SXS has the largest effective area above approximately 0.6 keV, giving a high sensitivity to faint X-ray sources.

## 5 In-orbit performance of the SXS

Figure 16 shows photos of the SXS Dewar and the ASTRO-H satellite. About one month after the launch, the satellite lost communication because of a problem in the attitude control system on the 26th of March 2016. Up until this accident, the SXS exhibited almost perfect performance in the orbit. Details about the in-orbit performances of the detector and the cooling system are reported in respective papers Eckart et al. (2018), Fujimoto et al. (2017), Noda et al. (2017), Ezoe et al. (2017), de Vries et al. (2017), Tsujimoto et al. (2017), Kilborne et al. (2017a, 2017b), Takei et al. (2017), Ishisaki et al. (2017), Porter et al. (2017), Shirron et al. (2018), Meng et al. (2018), Leutenegger et al. (2018), Sneiderman et al. (2018).

Energy resolution was continuously monitored using a radioactive calibration source, as shown in Fig. 17 (top). Mn K<sub>α1</sub> and K<sub>α2</sub> lines are clearly resolved, and the estimated energy resolution was 4.94 eV FWHM at 5.9 keV. This satisfies the requirement of 7 eV, and is the highest energy resolution ever achieved in X-ray astronomy at this energy.

In Fig. 17 (bottom), we show temperature curves measured at different positions on the He tank. The temperatures smoothly decreased to  $\sim 1.1$  K, as designed. Small

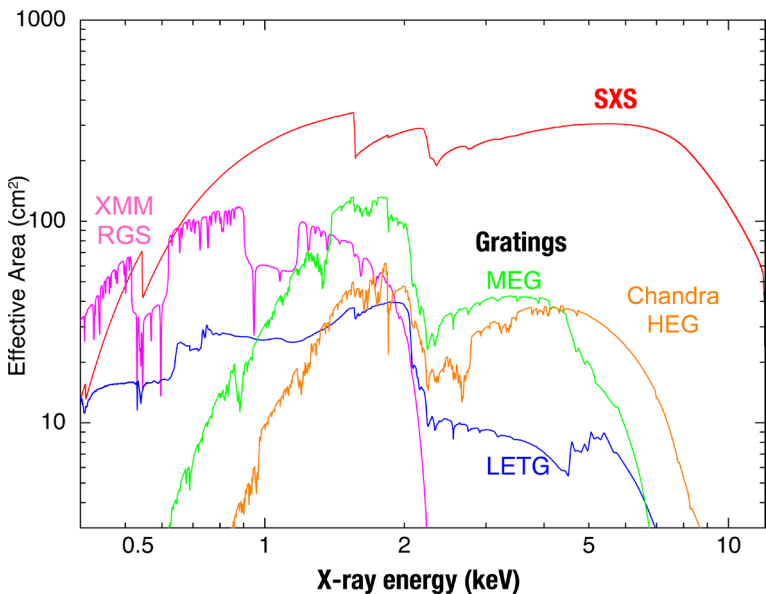


**Fig. 15** Effective area of the SXS and gratings onboard past X-ray astronomy satellites as a function of X-ray energy. Revised from the original figure in Mitsuda et al. (2010)

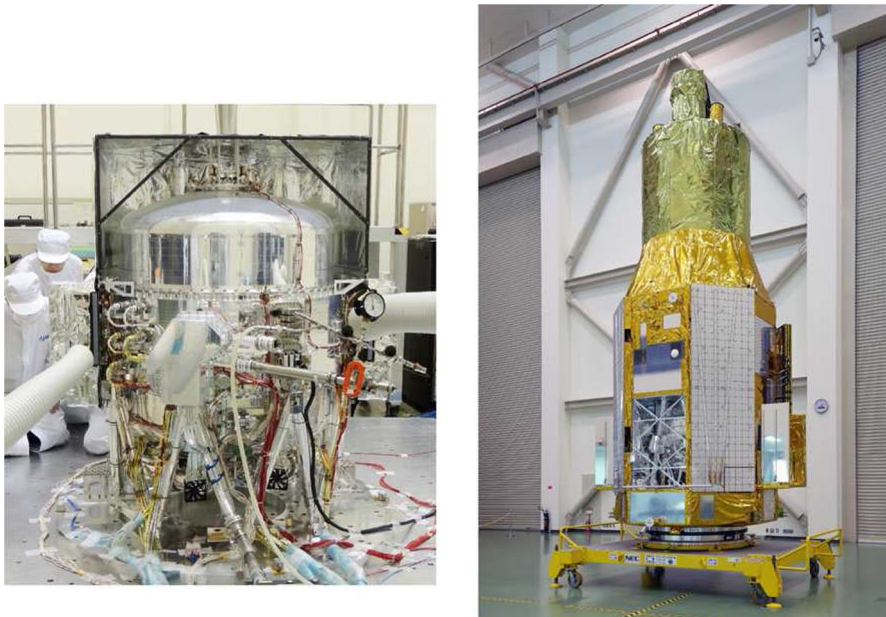


**Fig. 16** Photos of SXS Dewar and ASTRO-H satellite (Credit : JAXA).

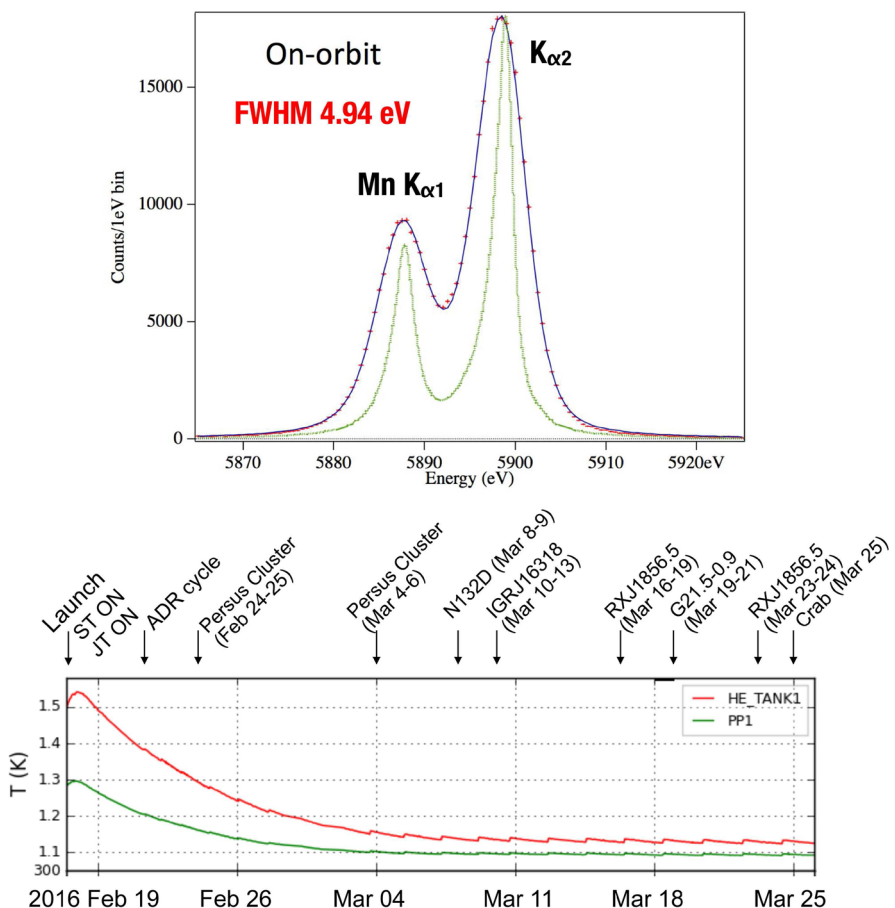


**Fig. 17** (Top) SXS spectrum of  $^{55}\text{Fe}$  calibration source on-orbit. The green line depicts the intrinsic line width of the source considering the natural width. The difference between the data and the intrinsic line width originates from instrumental line broadening. All pixel counts are summed Porter et al. (2017). (Bottom) On-orbit temperature profiles measured at different positions of the He tank. Arrows and texts indicate major operations and scientific observations Ezoe et al. (2017)

jumps observed at  $\sim 2$  day intervals in these profiles are due to ADR recycling to maintain the detector temperature at 50 mK. The temperature difference between the two curves is caused by the evaporation of liquid helium in the porous plug (PP), which is placed at the gas outlet hole of the dewar wall and separates the gas and liquid helium in zero gravity. Because of the latent heat of helium, the temperature measured at the PP is lower than that inside the He tank. All these instrument data confirm that SXS operate perfectly in orbit up till the accident of the satellite.

Even though the satellite was still in its initial commissioning phase, some scientific observations were successfully conducted, as labeled in Fig. 17. Observed sources are the Perseus cluster, N132D, IGR J16318-4848, RXJ1856.5-3754, G21.5-0.9, and the Crab Nebula. Examples of the observed energy spectra and images are

shown in Fig. 18. Among the observed objects, the most line rich spectrum was taken from the Perseus cluster. Emission lines from various elements, such as Si, S, Ar, Ca, Cr, and Fe are clearly detected. X-rays below 3 keV are overwhelmingly absorbed, because the gate valve had been kept closed. The gate valve is a cover put on the top of the dewar to protect thin filters inside the dewar on ground and at launch. It was planned to be opened after about 40 days after launch when the spacecraft outgassing becomes low enough to avoid contamination of the filters but this operation could not be conducted due to the short life time of the spacecraft. X-rays are thus subject to absorption by a 300  $\mu\text{m}$ -thick Be filter at the gate valve window.

Although these targets are observed mainly for in-orbit calibration of the instruments, these data can be used for scientific studies. A series of in-orbit calibration and scientific papers have been published in special sections of publications of SPIE and the Astronomical Society of Japan [70–72]. Below, we present highlights from the SXS results.

## 6 Scientific highlights from SXS results

### 6.1 Turbulence in the intracluster plasma

The Perseus cluster with a redshift  $z = 0.01756$  is a bright nearby cluster of galaxies. Like all other clusters, it contains X-ray emitting hot plasma and emits intense

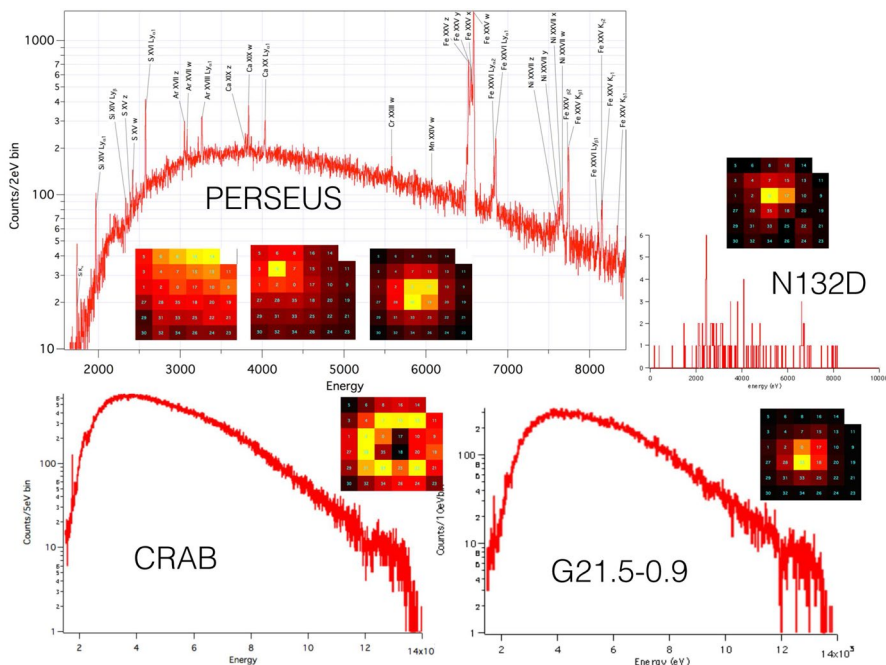


**Fig. 18** SXS spectra and images of observed astronomical objects Tsujimoto et al. (2016)

X-rays because of its short distance and high richness of the system. Figure 19 shows a magnified spectrum of the iron K line band (6.4–6.7 keV) for an area of  $\sim 60 \times 60$  kpc at the core of the Perseus cluster Collaboration (2016). The total exposure time is 230 ks. As compared with the Suzaku CCD spectrum, the SXS enabled, for the first time, separation of the major line components comprising the resonance, intercombination, and forbidden lines from the He-like iron Fe XXV.

The spectrum was fitted with Gaussians and a power-law continuum, where normalization and line widths of the Gaussian components were free. The center energies of the lines were fixed at redshifted laboratory values or theoretical values. The line widths were significantly broader than the instrumental response. We added in quadrature the expected thermal Doppler broadening of the Fe ions,  $83 \text{ km s}^{-1}$ , as implied by the ion temperature of  $\sim 4 \text{ keV}$  which is assumed to be the same as the measured electron temperature. This fit still failed to explain the observed line width, and an additional broadening due to the line-of-sight velocity dispersion (Gaussian  $\sigma$ ) by  $164 \pm 10 \text{ km s}^{-1}$  (90% confidence level) was required by the data. If this velocity dispersion mainly originates from the turbulent motion of the hot plasma in the core of the Perseus cluster, the turbulent pressure must be only  $\sim 4\%$  of the thermal pressure of this hot plasma with  $kT \sim 4 \text{ keV}$ .

A supermassive black hole in the central galaxy, NGC 1275, is thought to stir the intracluster medium by injecting jets. Previous Chandra images with high spatial resolution showed that two bubbles, with a diameter of about 10 kpc, are seemingly lifted up from the central supermassive black hole. This suggested a strong turbulence generated in the surrounding gas. However, the SXS observations indicate that the turbulence is in reality significantly milder, such that the turbulent plasma

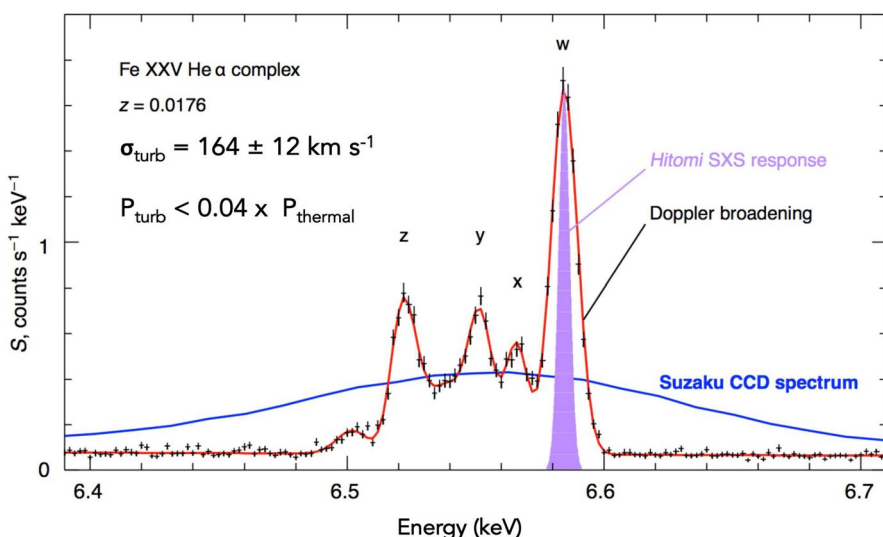


**Fig. 19** SXS spectrum of Perseus cluster core Collaboration (2016). The red curve depicts the best-fit power law and Gaussian model. The blue line depicts a Suzaku CCD spectrum. The purple line profile represents the SXS response with an energy resolution of 4.9 eV. Roman characters indicate line center energies of resonance (w), inter-combination (x, y), and forbidden (z) lines from He-like iron Fe XXV

motion exhibits considerably lower velocity than the ion sound velocity ( $1030 \text{ km s}^{-1}$  at  $kT = 4 \text{ keV}$ ). A puzzle remains on the scenario of AGN jets energizing the intracluster gas. Since the cooling time of the central gas is much shorter than the Hubble time, certain heating process needs to be at work to offset the gas cooling. Energy injected by the central AGN is unable to heat the cool-core region within the short cooling time, we need to find heating sources other than the AGN. Possibilities invoking such as cosmic rays, magnetic fields, galaxy motions, sound-wave heating and gas sloshing are under consideration Fabian et al. (2003), Gu et al. (2020), Ehlert et al. (2021). The SXS data have thus raised a new puzzle on the heating mechanism in the center of the cluster of galaxies.

The measured low value of the turbulent pressure also indicate that only a small correction is needed in the estimation of the gravitational mass of the cluster. To estimate the total mass of the cluster within a sphere of a given radius, the assumption of hydrostatic equilibrium is usually made, where the hydrostatic pressure balances the gravity as mentioned earlier. Although this assumption is widely applied in conventional X-ray data analysis of clusters and remains valid in the zeroth order approximation, additional pressures, such as turbulence or magnetic field, change the pressure balance leading to a larger mass estimations. At least as far as the turbulence is concerned, this uncertainty has been removed for this object.

A follow-up analysis showed the gas motion in the core in further detail by including data for an offset position Collaboration (2018a). The line widths of He-like and H-like ions of Si, S, Ar, Ca, and Fe indicated that the line-of-sight velocity shear is small,  $\sim 200 \text{ km s}^{-1}$  at maximum.

## 6.2 Fe-K line profile

Ion temperature can be measured from the line width assuming isotropic thermal motion of ions, with the superb energy resolution of the SXS. Here, the turbulent line broadening is independent of the atomic mass  $m$ , whereas the thermal Doppler width scales as  $\propto m^{-1/2}$ . Therefore, these two components can be separated by comparing line widths for several different elements. The ion temperature thus constrained is  $7.3_{-5.0}^{+5.3} \text{ keV}$  if the most secure seven line measurements at more than  $10\sigma$  significance are used where errors are given at 68% confidence levels. All ion species are assumed to have the same value of the ion temperature. The obtained value is in good agreement with the electron temperature determined from the spectral continuum of  $\sim 4 \text{ keV}$  Collaboration (2018a, 2018b, 2018c). This is the first observational constraint of the ion temperature for the intracluster medium.

Further, the resonance ( $w$ ) line of the He-like Fe ion is found to be significantly weaker by about 30% than the CIE model prediction, indicating that the gas is optically thick to the resonant scattering Collaboration (2018a). The spectral analysis shows that a slightly broader line shape of the  $w$  line and its flux are consistent with a spherical plasma whose optical depth to the resonant scattering is  $\gtrsim 2$ . The presence of the resonance scattering is also consistent with the observed level of the weak turbulence, since strong turbulence would suppress the resonance scattering effect.

### 6.3 Chemical abundance

Besides the kinematics of the diffuse plasma of the Perseus cluster, the SXS allowed a search for weak emission lines that have not been well constrained by the past missions Collaboration (2017a). Figure 20 shows magnified spectra and abundance ratios of heavy elements relative to Fe.

Despite the weak line signals, lines from Cr, Mn, and Ni are clearly detected with the SXS, as shown in the top-left and -right panels of Fig. 20. Further, as shown in the top-right panel of Fig. 20, the SXS results for Cr, Mn, and Ni abundances are lower by a factor of 1.5–2 than the previous XMM-Newton values determined with CCDs. This is partly due to an update of the theoretical model, but there is undoubtedly a large systematic error in the CCD measurement of very weak lines. Thus, the clear detection of weak lines with the SXS has provided unambiguous abundance values for the Fe-peak elements.

These heavy elements are synthesized by billions of supernovae in the constituent galaxies and expelled into the cluster space. The abundance ratios of the Fe-peak elements thus can constrain how typical type Ia supernovae occurred in elliptical galaxies which are most abundant in rich clusters of galaxies. Two most frequently discussed possibilities are single-degenerate (SD) and double-degenerate (DD) channels. In the SD channel, a white dwarf accretes matter from a non-degenerate companion star, and its mass increases to a near-Chandrasekhar limit. The Chandrasekhar mass, about  $1.4M_{\odot}$ , is the maximum level for a stable white dwarf, supported by electron degeneracy pressure holding against gravity. The white dwarf at this mass would ignite various unstable nuclear reactions leading to a type Ia supernova. In contrast, in the DD channel, double white dwarfs with masses below the Chandrasekhar limit undergo unstable mass transfer to coalesce and result in type Ia supernova. If SD or DD origin of type Ia supernova is sorted out, we can quantify how Fe-peak elements are enrichment in the past and in future. Since all supernova explosions will shift to type Ia in the long future, this knowledge would be important to see how our Universe will chemically evolve. Also, because type Ia supernovae are used as a standard candle for precision cosmology to measure the distance to their host galaxies, the nature of the progenitor system is important.

One important question is, therefore, whether the mass of the exploding white dwarf is near the Chandrasekhar limit (Near- $M_{\text{ch}}$ ) or below it (Sub- $M_{\text{ch}}$ ). These two scenarios predict difference in the production efficiency of neutron-rich species like Ni and Mn, because only in the Near- $M_{\text{ch}}$  scenario the white dwarf core is sufficiently dense to enable electron capture in the initial phase of explosion.

Comparison between the results and nucleosynthesis calculations suggests that the measured Mn/Fe and Ni/Fe ratios are significantly higher than the Sub- $M_{\text{ch}}$  scenario, but slightly smaller than the Near- $M_{\text{ch}}$  one as shown in the bottom panel of Fig. 20. Therefore, a combination of SD and DD processes would contribute to type Ia supernova, resulting a near-solar abundances for all the elements. It is also a surprise that the solar abundance is held in such a different environment from the solar neighborhood. This might suggest that our Galaxy including the solar system and the Perseus cluster experienced a similar star formation history and thus the

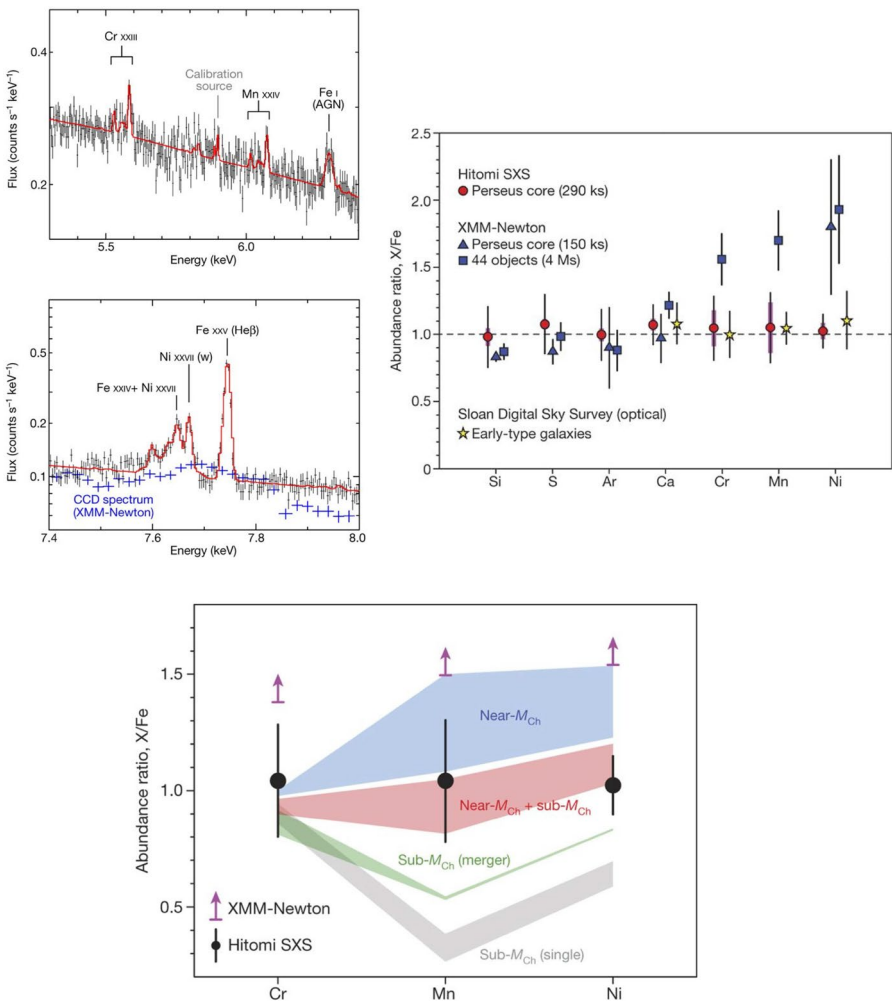


**Fig. 20** Detections of weak emission lines and abundance ratios to Fe in Perseus cluster core region Collaboration (2017a). (Left top) Magnified spectrum in 5.3–6.4 keV, where He-like Cr and Mn K lines are detected. The red line shows a modeled spectrum using an optically thin thermal plasma and atomic data base values. (Left middle) Same as the left top panel, but for 7.4–8.0 keV, where a Ni XXVII resonance line is detected. Blue data points indicate an XMM Newton CCD spectrum for the same region. (Right top) Chemical abundance of heavy elements constrained from the SXS spectrum. Blue marks correspond to past observations with X-ray CCDs onboard the XMM-Newton satellite. Stars indicate chemical abundance of early-type galaxies obtained in the Sloan Digital Sky Survey in the optical wavelength range. (Bottom) Same as the right top panel, but for Cr, Mn, and Fe. Magenta arrows indicate a  $1\sigma$  lower limit of the XMM-Newton measurements for 44 regions. Blue, green, and gray regions are theoretical predictions for type Ia supernova. The red region is a model assuming equal contributions from Near- $M_{\text{ch}}$  type Ia supernova and Sub- $M_{\text{ch}}$  violent mergers

chemical abundance of the solar system follows to the nature of the average type Ia supernova in the Universe.

#### 6.4 Search for unidentified line emission and absorption

Another interesting result is obtained from the search of unidentified line emission in the Perseus cluster spectrum. Previously, a weak 3.5 keV line feature from a stacked sample of clusters of galaxies was noticed and examined in the X-ray CCDs spectra obtained with the XMM-Newton satellite Collaboration (2017b), Tamura et al. (2019). Such emission line signals may originate from radiative decay of keV sterile neutrinos, which are a dark matter candidate, since clusters are regarded as massive dark matter structure.

Figure 21 shows the SXS spectrum of the Perseus cluster core around 3.5 keV. The SXS results show no significant emission nor absorption lines where the unidentified line was claimed to appear (blue and red brackets), and the upper limit on the line flux is converted to the decay rate of the hypothetical dark matter particles. The previous report of the emission line feature at 3.5 keV from this cluster has been ruled out. A hint of a broad excess near the energies of S XVI ( $E \simeq 3.38$  keV

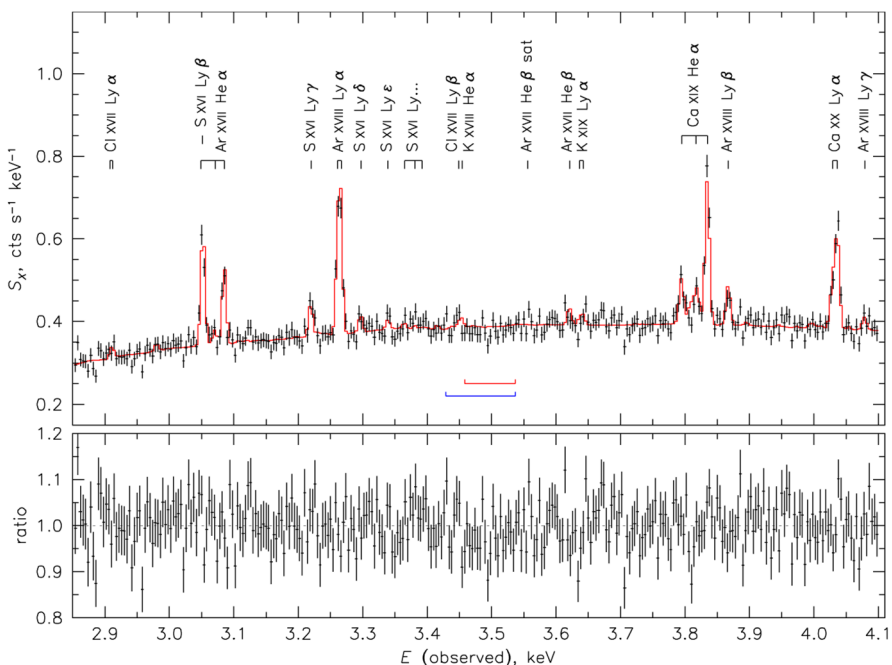


**Fig. 21** SXS spectrum of Perseus cluster core. Energies are shown in the observer frame. A red solid line in the top panel represents a best-fit CIE plasma model. The bottom panel depicts a ratio of the data to the best-fit model. Red and blue brackets show 90% confidence intervals on the 3.5 keV line energy for the XMM-Newton stacked-cluster sample and for the XMM-Newton Perseus cluster, respectively Collaboration (2017b)

as the measured energy) is observed, and it suggests a possible signature of charge exchange between heavy ions and molecular clouds in the Perseus cluster. This may explain the unidentified line around 3.5 keV. This possibility has been suggested before Gu et al. (2015) with CCD observations but can be more accurately examined by future observations with high spectral resolution.

The SXS has a small grasp, i.e. the FOV multiplied by the effective area, which is a measure of the sensitivity to diffuse X-ray sources. This and the short exposure time limit the sensitivity to the unidentified line feature. In spite of these difficulties, these results demonstrate that the X-ray microcalorimeter observations will be able to constrain decay emission from massive dark matter structures in the Universe more efficiently than the previous instruments.

## 6.5 Atomic data and plasma codes

The SXS spectrum of the Perseus cluster with  $\sim 5$  eV resolution, comprising numerous emission lines, offers an unprecedented opportunity to test theoretical models of X-ray emission from hot collisional plasmas Collaboration (2018c). Spectral model for a hot plasma takes into account various components: in particular, ionization balance, transition energies, and their oscillator strengths are major factors affecting the reliability of the spectral model. The observed spectrum of the Perseus cluster is dominated by the CIE plasma emission modeled by the plasma codes, as expected from the  $n_e t$  value greater than  $3 \times 10^{12} \text{ cm}^{-3} \text{ s}$  in the intracluster space. Contribution from the central AGN, NGC 1275, to the spectrum can be ignored.

The frequently applied plasma codes in the spectral fits were tested: AtomDB/APEC Smith et al. (2001), Foster et al. (2012), SPEX Kaastra et al. (1996), and CHIANTI Dere et al. (1997), Del Zana et al. (2015). Figure 22 compares the best-fit models of different plasma codes for the observed Perseus spectrum in the He-like Fe line band. Although these models reproduce the overall shape of the data fairly well, clear differences exist among the codes. In this plot, the baseline model is a post-launch version of SPEX (v3.03) updated to give a good fit to the observed Fe K-line spectrum with the SXS Collaboration (2016).

The systematic deviations among the codes originate from the atomic data employed in individual models, namely ionization balance, collisional excitation/de-excitation rates, recombination rates, transition probabilities, and other effects. These differences result in systematic uncertainties in the derived physical parameters of the hot plasma, including the emission measure, temperature, line-of-sight velocity dispersion, elemental abundances, column density of the absorbing matter, and redshift. For example, the best-fit temperature of the base-line model is  $3.969 \pm 0.017$  keV, with the statistical error being  $1\sigma$ . The best-fit temperatures with different models vary by  $\sim 10\%$ , which is not a negligible difference.

In examining the plasma codes, it is important to use them in a proper astrophysical context. For this purpose, astrophysical conditions, such as non-equilibrium and multi-temperature, need to be taken into account Collaboration (2018c). In the base-line model, a single temperature is assumed for the hot plasma in the Perseus cluster core. However, the Perseus cluster core exhibits both temperature and abundance

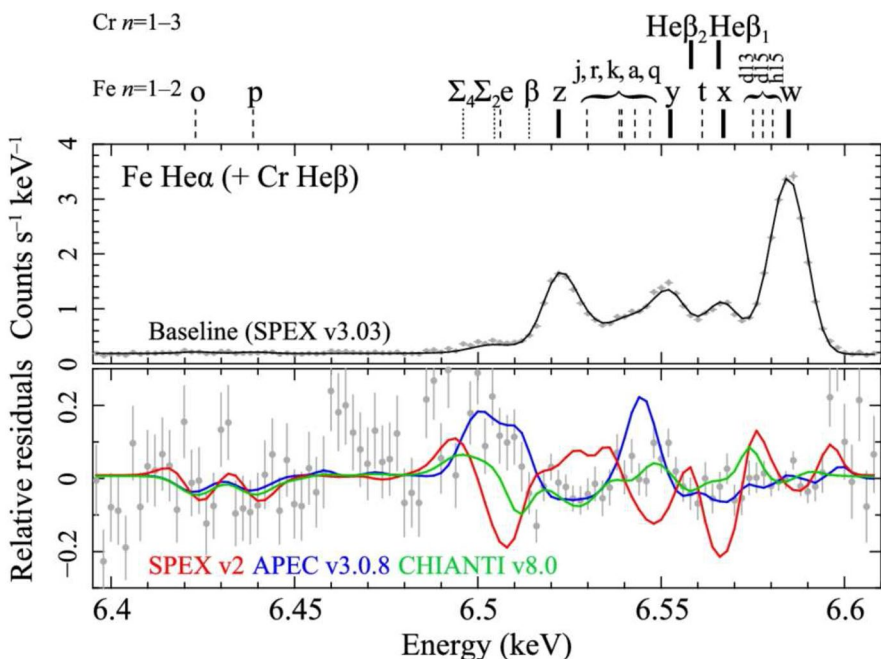


**Fig. 22** SXS spectrum of Perseus cluster in He-like Fe K band Collaboration (2018c). The upper panel shows the data with the best-fitted model depicted as a solid line. The lower panel shows residuals,  $(\text{data} - \text{model})/\text{model}$ , and relative differences between the base-line model (SPEX v3.03) and other plasma codes. Labels indicate center energies of emission lines from Cr and Fe ions

gradients. A 3-temperature CIE model (3CIE) was thus tested and it improved the C-statistics over the 1CIE and 2CIE cases, where common abundances of Si, S, Ar, Ca, Cr, Mn, Fe, and Ni were assumed for the three temperature components. The obtained temperatures are  $1.92 \pm 0.21$ ,  $3.61 \pm 0.33$ , and  $5.43 \pm 0.38$  keV, respectively. The multi-temperature feature should reflect the following factors: (i) temperature gradient within the SXS FOV ( $\sim 60 \times 60$  kpc) is not resolved, (ii) the ICM temperature changes significantly along the line of sight, (iii) there can be a small-scale fluctuation of temperature unresolved with SXS, and (iv) multiple plasma components with distinct temperatures can exist cospatially. The major component shows a temperature around 3 keV, reflecting a relatively cold gas within 10 kpc from the cluster center than the  $\sim 6$  keV observed for larger radii.

Contributions of charge exchange between neutrals and charged ions is also considered. High- $n$  transitions for SXVI and FeXXV are seen at  $\sim 3.4$  keV and  $\sim 8.6$  keV, respectively. The former is the same as that described before in searching for unidentified line. Including the charge exchange component results in a minor improvement of the spectral modeling.

These studies strongly suggest that modeling of astrophysical plasma including all the astrophysical conditions is crucial in deriving correct physical parameters even from a high resolution X-ray spectrum. To make it possible, the X-ray astronomy community is collaboratively working for accurate and complete atomic data

and plasma models. We hope that all the necessary atomic data will be installed soon in the plasma codes, along with the systematic uncertainties of the models, especially in major emission or absorption line structures. Then, the reliability of the model will be strengthened by fitting into high-resolution spectra for various astronomical objects with the energy resolution comparable to that of the SXS.

## 7 Beyond ASTRO-H

Despite the short lifetime of ASTRO-H, novel observational results were obtained with the X-ray microcalorimeter, as described above. The detector and the cooling system functioned very well until the loss of the satellite, which makes the loss of the satellite all the more regrettable. On the other hand, there are numerous difficulties met by the team during the SXS development and all the effort to solve them brought valuable knowledge to be exercised for the next chance. We believe that the microcalorimeters will operate smoothly in future missions. Here, we describe two accepted missions, which aim for high-resolution spectroscopy, using microcalorimeters.

### 7.1 XRISM

We first describe the X-Ray imaging spectroscopy mission (XRISM), which is a Japanese-US astronomy project to be conducted in collaboration with Canada and European countries Tashiro et al. (2018). Following the loss of ASTRO-H, this recovery program was initiated by JAXA and NASA, who considered that the new science which can only be carried out by microcalorimeters has the utmost importance. The main purpose of this mission is another challenge of the high-resolution X-ray spectroscopy originally aimed at by the ASTRO-H SXS. Hard X-ray and soft gamma-ray studies, the other main feature of ASTRO-H, will be considered for separate future mission, due mainly to the available resource for XRISM.

The main scientific objectives of XRISM are in accordance with those of ASTRO-H, but are redefined to focus on the X-ray microcalorimeter science; (1) investigation of large scale structures of the Universe and evolution of clusters of galaxies through gas dynamics studies in various types of clusters of galaxies (dynamically relaxed clusters and mergers) and precise mass measurements with tight constraints on gas motions, (2) chemical evolution of the Universe through measurements of elemental abundances, the velocity dispersion of SNRs, and outflows from galaxies, (3) energy transportation and feedback in the Universe from abundance and velocity measurements of outflows from galaxies and AGNs, and (4) exploration of new science with high-resolution spectroscopy XRISM Science Team (2020). These scientific purposes reflect what have been achieved with the SXS, as described in Sect. 6, and will further expand them to a number of cosmic X-ray sources.

Figure 23 shows the concept of the XRISM satellite. Its design is, to a large extent, inherited from ASTRO-H, with smaller number of instruments than ASTRO-H as mentioned above. The X-ray microcalorimeters and X-ray CCDs are both

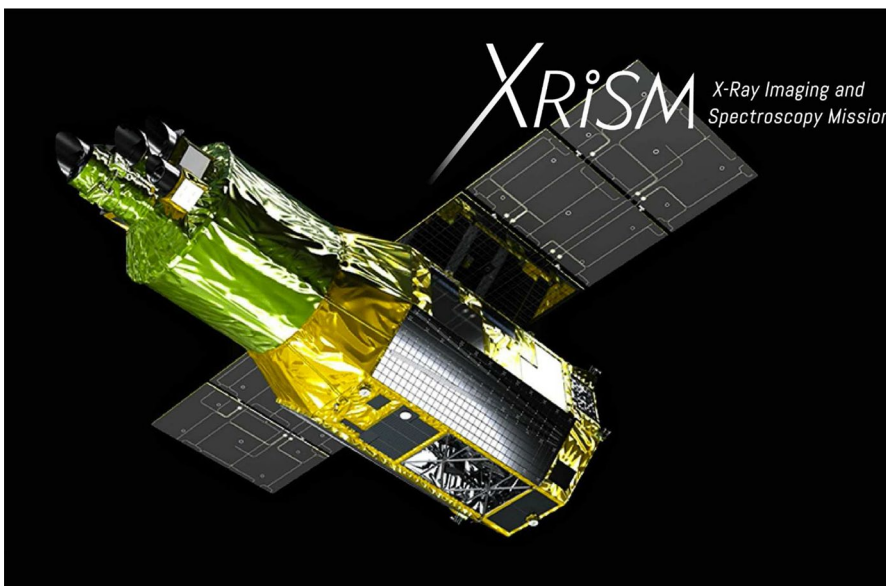


**Fig. 23** X-ray astronomy satellite XRISM [91]

equipped with individual X-ray mirror assemblies. Even though it is basically a rebuild of the ASTRO-H satellite, certain changes in the satellite system and in the instrument design will be introduced based on the lessons learned; namely, improvement of the attitude control system to avoid anomalous events that occurred in ASTRO-H, a new baffle placed on top of the microcalorimeter dewar to protect the thin blocking filters in the aperture cone against micrometeorites and orbital debris. The X-ray microcalorimeter system, including its X-ray mirror assembly, is now named “Resolve” to represent the strong will of the team. The X-ray CCDs with its X-ray mirror assemblies are named Xtend. The XRISM satellite is expected to be launched in the early 2020s.

Because of the short lifetime of ASTRO-H, a wide range of scientific targets planned for the ASTRO-H mission remain unobserved and will be studied with XRISM. Most of the planned observations in the early phase of ASTRO-H are described in ASTRO-H white papers [92], in which 16 papers address all the categories of X-ray sources. We would like to work on these ASTRO-H scientific challenges as soon as possible and thereby aim to revise our understanding of X-ray emitting sources.

As described in Sect. 3, the high resolution X-ray spectroscopy of the XRISM will contribute to modern plasma physics in numerous ways. The results from ASTRO-H, in particular for the Perseus cluster of galaxies, give some updates on the observing program in the early phase of the mission. Significant detection of turbulence, at a moderate level, from the Perseus cluster demonstrated the importance of a systematic study of gas dynamics in clusters of galaxies. XRISM program plans long observations for a few bright clusters with different morphologies such

as presence or absence of dominant galaxy in the center. We hope the XRISM study will give clear answer to the role of AGN, as well as of other sources, in supplying energy to the intracluster gas. Strategy for supernova remnants has science related to plasma processes as one key goal. XRISM will measure gas velocity, temperatures of electrons and ions, as well as ionization levels, all separately. We will visualize how energy is transported in collisionless shocks between electrons and ions, ionizing or recombining features of non-equilibrium plasmas, and presence of charge exchange process where hot and cold gas make a contact. These studies will be supported by the revised atomic code, valuable outcome from the ASTRO-H observations. Even though the XRISM mission will operate with more than five years delay from ASTRO-H, its science will be strengthened by assembling what we have learned from ASTRO-H. We hope that these astrophysical studies will contribute to general plasma physics as well from various aspects such as how the turbulence in compressive fluids is created, transported and dissipated and how shocks in collisionless plasma is formed and charged particles gain energy.

## 7.2 Athena and beyond

Another future mission we introduce here is the European Space Agency (ESA)-led Athena (Advanced Telescope for High-ENergy Astrophysics), which will greatly advance the high-resolution spectroscopy [93]. Its launch is planned shortly after 2030. The Athena mission has been approved by ESA, and major part of the satellite development and its launch is under ESA's responsibility. However, contributions on the instrument development and science study are being made from NASA and JAXA. The satellite has one unit of large X-ray telescope, whose focal plane is shared by two types of detectors. One detector employs semiconductor active pixel sensors (Wide-Field Imager: WFI), and the other consists of advanced type X-ray microcalorimeters and named X-ray Integral Field Unit (X-IFU) [94].

The microcalorimeters for the X-IFU instrument are so-called transition edge sensor (TES) microcalorimeters, advanced version of the SXS type sensors. In TES, the thermometer is made of a thin metal bilayer, which makes a superconducting transition at a specified temperature defined by the layer thickness. The sensor is voltage biased to operate in the middle of the normal to super transition edge Irwin and Hilton (2005). TES exhibits a large gradient of electric resistance with temperature, compared with the semiconductor thermometer. This results in a significantly better energy resolution, 2.5 eV or better at 5.9 keV, and a shorter time constant of the signal than the SXS practice. This requirement on the spectral resolution at this energy band (2.5 eV) is defined to achieve high line sensitivity and precise velocity determination ESA (2016). Furthermore, a larger pixel array can be produced using multiplexing readout of TES pixels. The number of pixels will be approximately 3600, which is two orders of magnitude larger than those of the SXS. The effective area and angular resolution of the telescope for Athena are approximately 1 m<sup>2</sup> at 1 keV and less than 10 arcseconds, respectively. With Athena, good photon statistics will be available at significantly shorter exposure times along with high spatial resolution than the ASTRO-H SXS and the XRISM Resolve. Figure 24 shows an

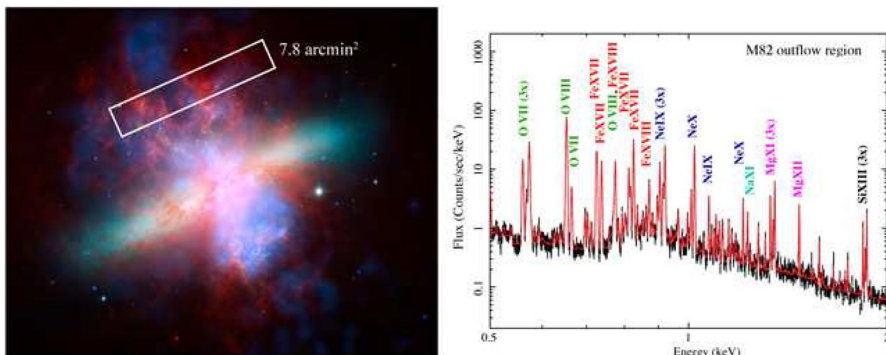


**Fig. 24** (Left) Composite image of M82 (X-rays in blue, hydrocarbon emission at  $8 \mu$  in red, optical starlight in cyan, and  $H_{\alpha} + [NII]$  in yellow). (Right) 100 ks simulated Athena TES spectrum of the M82 outflow as indicated by a box in the left panel Athena assessment study report (2011)

example of a simulated X-ray spectrum of a galactic outflow produced by supernova activity in the starburst galaxy M82. Chemical composition and velocity of the outflow will show the total kinetic energy and the amount of heavy elements injected from galaxies to the intergalactic space in the evolution of galaxies.

Finally, even though the present microcalorimeters have superb resolving power for a wide energy range, there are important scientific phenomena that require even higher resolution and better imaging capability. For example, most of the baryonic matter in the local Universe remains undetected, as mentioned earlier. It is predicted that these “dark baryons” exist as tenuous warm-hot ( $10^{5-6}$  K) plasmas outside of galaxies and clusters. To detect faint X-ray emission from these plasmas which should emit soft X-rays mainly below 2 keV, a wider field-of-view ( $\sim 30' \times 30'$ ), with  $\sim 10$  arcsec resolution, and a better energy resolution ( $\lesssim 2$  eV in FWHM at 0.6 keV) than the SXS ( $\sim 3' \times 3'$  and  $\sim 5$  eV) are required (e.g., Ohashi et al. (2014)). This is technically feasible by adopting TES microcalorimeters combined with a new readout method, employing microwave multiplexing technique. The distribution of dark baryons and their thermal and chemical properties would bring us rich information about the cosmological evolution of matter and possibly about the basics physics of tenuous collisionless plasmas.

## 8 Summary

Our Universe provides us with enormous variety of astrophysical plasmas, whose parameter ranges, such as density, temperature, magnetic field, and spatial scale, are far greater than what can be achievable in the laboratory. The knowledge obtainable from astrophysical plasmas is unique and fundamental to the physics, and it is of great importance to perform accurate measurement of the plasma properties through their radiation characteristics. For this purpose, high-resolution X-ray spectroscopy is a powerful method and the technology is rapidly improving in recent years. The history of X-ray astronomy over 60 years has brought us dramatic improvement of

spectral resolution, along with the development of angular resolution and polarimetry capability. X-ray microcalorimeters give us unparalleled capabilities, with the superb energy resolution, high quantum efficiency, and applicability to extended sources, all fulfilled simultaneously. The ASTRO-H SXS, equipped with the first microcalorimeters onboard, has brought us a marvelous view of the spectroscopic universe even with its short lifetime. We are convinced that X-ray astronomy is still full of possibilities and surprises. We hope that future X-ray spectroscopy missions, including XRISM and Athena, will greatly deepen our understanding of astrophysical plasmas and change our view of the Universe.

**Acknowledgements** The authors deeply thank the organizers of the 2nd Asia-Pacific Conference on Plasma Physics for giving us this opportunity to describe this paper, and also thank the editors, anonymous reviewers, and Dr. Magnus Axelsson for useful comments and suggestions. We are also really grateful for all the SXS team and the ASTRO-H team. We thank the Japanese SXS team members, in particular Dr. Yoshitaka Ishisaki, Dr. Ryuichi Fujimoto, Dr. Yoh Takei, Dr. Noriko Y. Yamasaki, Dr. Masahiro Tsujimoto, Dr. Hiroya Yamaguchi, Dr. Mina Ogawa, Dr. Shu Koyama, Dr. Hiroyuki Sugita, Dr. Yoichi Sato, Dr. Keisuke Shinozaki, Dr. Atsushi Okamoto, Dr. Kumi Ishikawa, Dr. Makoto Sawada, Dr. Naoko Iyomoto, Dr. Shinya Yamada, Dr. Hiromi Seta, Dr. Masahide Murakami, Dr. Yoichi Yatsu, Dr. Kyoko Matsushita, Dr. Kosuke Sato, Dr. Hiroshi Murakami, Dr. Hirofumi Noda, Dr. Ikuyuki Mitsuishi, Dr. Naomi Ota, Dr. Toru Tamagawa, Dr. Toshiki Sato, Dr. Shunji Kitamoto, Dr. Yukikatsu Terada, and Dr. Makoto Tashiro. We are grateful for the US SXS team members led by Dr. Richard L. Kelley, who is the Principal Investigator of the US SXS team that includes Dr. Caroline A. Kilbourne, Dr. Scott F. Porter, Dr. Gary A. Neiderman, Dr. Michael DiPirro, Dr. Peter Shirron, Dr. Gregory V. Brown, Dr. Andrew Szymkowiak, and Dr. Dan MacCannan as well as the ESA members, including Dr. Jan-Willem den Herder and Dr. Stephane Paltani. Other than these scientists and engineers from universities and research institutes, commercial companies have contributed their effort towards the SXS instrument for years. Further, more people were involved in the development of the other instruments onboard ASTRO-H, the spacecraft, and scientific studies. We also thank these members. The results presented here are fruits of a long-standing desire to make this instrument realize. From this point of view, the microcalorimeter instrument onboard the recovery mission XRISM is appropriately called “Resolve”. We also appreciate all the XRISM team members for their on-going great efforts in the development of the instruments and the spacecraft.

**Open Access** This article is licensed under a Creative Commons Attribution 4.0 International License, which permits use, sharing, adaptation, distribution and reproduction in any medium or format, as long as you give appropriate credit to the original author(s) and the source, provide a link to the Creative Commons licence, and indicate if changes were made. The images or other third party material in this article are included in the article's Creative Commons licence, unless indicated otherwise in a credit line to the material. If material is not included in the article's Creative Commons licence and your intended use is not permitted by statutory regulation or exceeds the permitted use, you will need to obtain permission directly from the copyright holder. To view a copy of this licence, visit <http://creativecommons.org/licenses/by/4.0/>.

## References

- ASTRO-H CookBook Members, “ASTRO-H Cook Book - A First Step to ASTRO-H Spectral Analysis”, rev 1.0, Japan (2015)
- ASTRO-H White Paper, <https://arxiv.org/html/1412.2351>
- Athena assessment study report, “Athena The extremes of the Universe: from black holes to large-scale structure”, ESA/SRE(2011)17 (2011)
- H. Böhringer, N. Werner, X-ray spectroscopy of galaxy clusters: studying astrophysical processes in the largest celestial laboratories. *Astron. Astrophys. Rev.* **18**, 127 (2010)

- H.V.D. Bradt, T. Ohashi, K.A. Pounds, X-ray astronomy missions. *Annu. Rev. Astron. Astrophys.* **30**, 391 (1992)
- E. Branchini et al., Studying the warm hot intergalactic medium with Gamma-Ray bursts. *Astrophys. J.* **697**, 328 (2009)
- G. Branduardi-Raymont et al., AXIOM: advanced X-ray imaging of the magnetosphere. *Exp. Astron.* **33**, 403 (2012)
- China National Space Administration, <http://www.cnsa.gov.cn/english/> (2019)
- G.W. Clark, “*Bruno Benedetto Rossi 1903–1993*”, *National Academy of Sciences* (National Academy Press, 1998)
- C.P. de Vries et al., Calibration sources and filters of the soft x-ray spectrometer instrument on the Hitomi spacecraft. *J. Astron. Telescopes Instr. Sci.* **4**, 011204 (2017)
- G. Del Zanna et al., CHIANTI—an atomic database for emission lines. Version 8. *Astron. & Astrophys.* **582**, A56 (2015)
- K. Dennerl, Charge transfer reactions. *Space Sci. Rev.* **157**, 57 (2010)
- Department of Space, Indian Space Research Organization, <https://www.isro.gov.in> (2019)
- K.P. Dere et al., CHIANTI—an atomic database for emission lines. *Astron. & Astrophys.* **125**, 149 (1997)
- M. Eckart et al., Ground calibration of the Astro-H (Hitomi) soft x-ray spectrometer. *J. Astron. Telescopes Instrr. Sci.* **4**, 021406 (2018)
- K. Ehlert et al., Connecting turbulent velocities and magnetic fields in galaxy cluster simulations with active galactic nuclei jets. *MNRAS* **503**, 1327 (2021)
- ESA, “Athena Science Requirements Document”, SRE-S/ATH/2015/01, 1.5 (2016)
- ESA Athena Home Page, <http://sci.esa.int/athena/>
- ESA Science and Technology, <https://sci.esa.int> (2019)
- Y. Ezoe et al., Enhancement of terrestrial diffuse X-ray emission associated with coronal mass ejection and geomagnetic storm. *Publ. Astron. Soc. Jpn.* **63**, 691 (2011)
- Y. Ezoe et al., Porous plug phase separator and superfluid film flow suppression system for the Soft X-ray Spectrometer onboard Hitomi. *J. Astron. Telescopes Instr. Sci.* **4**, 011203 (2017)
- Y. Ezoe et al., Ultra light-weight X-ray telescope missions : ORBIS and GEO-X. *J. Astron. Telescope Instrum* **4**, 046001 (2018)
- A.C. Fabian et al., A deep Chandra observation of the Perseus cluster: shocks and ripples. *MNRAS* **344**, L43 (2003)
- A.C. Fabian et al., A wide Chandra view of the core of the Perseus cluster. *MNRAS* **418**, 2154 (2011)
- A.R. Foster et al., Updated atomic data and calculations for X-ray spectroscopy. *Astrophys. J.* **756**, 128 (2012)
- R. Fujimoto et al., Performance of the helium dewar and the cryocoolers of the Hitomi soft x-ray spectrometer. *J. Astron. Telescopes Instrr. Sci.* **4**, 011208 (2017)
- Y. Fukazawa et al., Metal concentration and X-ray cool spectral component in the central region of the Centaurus cluster of galaxies. *PASJ* **46**, L55 (1994)
- M. Fukugita, P.J.E. Peebles, The cosmic energy inventory. *Astrophys. J.* **616**, 643 (2004)
- M. Fukugita, C.J. Hogan, P.J.E. Peebles, The cosmic baryon budget. *Astrophys. J.* **503**, 518 (1998)
- R. J. Gabany, “Galaxies of the Perseus Cluster”, <http://apod.nasa.gov/apod/ap090508.html> (2009)
- K.V. Getman et al., Membership of the Orion Nebula population from the Chandra Orion untradeep project. *Astrophys. J. Suppl.* **160**, 353 (2005)
- R. Giacconi et al., Evidence for X rays from sources outside the solar system. *Phys. Rev. Lett.* **9**, 439 (1962)
- R. Giacconi, History of X-ray telescopes and astronomy. *Exp. Astron.* **25**, 143 (2009)
- R. Giacconi, H. Gursky, *X-Ray Astronomy* (Springer, Berlin, 1974)
- L. Gu et al., A novel scenario for the possible X-ray line feature at  $\sim$ 3.5 keV. *A&A* **584**, L11 (2015)
- L. Gu et al., Implications of the mild gas motion found with Hitomi in the core of the Perseus cluster. *Astron. Astrophys.* **638**, A138 (2020)
- M. Güdel, Y. Nazé, X-ray spectroscopy of stars. *Astron. Astrophys. Rev.* **17**, 309 (2009)  
<http://xrism.isas.jaxa.jp>
- <https://academic.oup.com/pasj/issue/70/2>
- <https://www.spiedigitallibrary.org/journals/Journal-of-Astronomical-Telescopes-Instruments-and-Systems/volume-4/issue-1>
- <https://www.spiedigitallibrary.org/journals/Journal-of-Astronomical-Telescopes-Instruments-and-Systems/volume-4/issue-2>

- Hitomi Collaboration, The quiet intracluster medium in the core of the perseus cluster. *Nat. Lett.* **535**, 117 (2016)
- Hitomi Collaboration, Solar abundance ratios of the Iron-Peak elements in the Perseus Cluster. *Nature* **551**, 478 (2017)
- Hitomi Collaboration, Hitomi constraints on the 3.5 keV line in the Perseus galaxy cluster. *Astrophys. J.* **837**, L15 (2017)
- Hitomi Collaboration, Measurements of resonant scattering in the Perseus Cluster core with Hitomi SXS. *Publ. Astron. Soc. Jpn.* **70**, 10 (2018)
- Hitomi Collaboration, Atmospheric gas dynamics in the Perseus cluster observed with Hitomi. *J. Astron. Telescopes Instrr. Sci.* **70**, 9 (2018)
- Hitomi Collaboration, Atomic data and spectral model constraints from high-resolution X-ray observations of the Perseus cluster with Hitomi. *Publ. Astron. Soc. Jpn.* **70**, 12 (2018)
- K. Irwin., C. Hilton, “Transition-Edge Sensors”, *Topics Appl. Phys.* **99**, 63 (2005)
- Y. Ishisaki et al., In-flight performance of pulse-processing system of the ASTRO-H/Hitomi soft x-ray spectrometer. *J. Astron. Telescopes Insrtr. Sci.* **4**, 011217 (2017)
- JAXA <https://global.jaxa.jp> (2019)
- J.S. Kaastra et al., “ASTRO-H White Paper - AGN Winds”, astro-ph, [arXiv:1412.1171](https://arxiv.org/abs/1412.1171) (2014)
- J.S. Kaastra, R. Mewe., H. Nieuwenhuijzen, in UV and X-ray Spectroscopy of Astrophysical and Laboratory Plasmas , ed. Yamashita K., Watanabe T. (Universal Academy Press: Tokyo), 411 (1996)
- J.S. Kaastra et al., Thermal radiation processes. *Space Sci. Rev.* **134**, 155 (2008)
- T.R. Kallman et al., Photoionization modeling and the K Lines of Iron. *Astrophys. J. Supplement Ser.* **155**, 675 (2004)
- S. Katsuda et al., High-resolution X-ray spectroscopy of the galactic supernova Remnant Puppis a with the XMM-Newton RGS. *ApJ* **756**, 49 (2012)
- C. Kilborne et al., Design, implementation, and performance of the Astro-H SXS calorimeter array and anticoincidence detector. *J. Astron. Telescopes Insrtr. Sci.* **4**, 011214 (2017)
- C. Kilborne et al., Design, implementation, and performance of the Astro-H soft x-ray spectrometer aperture assembly and blocking filters. *J. Astron. Telescopes Insrtr. Sci.* **4**, 011215 (2017)
- K. Kobayashi et al., The marshall grazing incidence X-ray spectrometer (MaGIXS). *Proc. SPIE* **10699**, 1069927 (2018)
- J. Kormendy, D. Richstone, “Inward Bound—The Search For Supermassive Black Holes In Galactic Nuclei”, *Annual Rev. Astron. Astrophys.*, 33, 581 (1995)
- M.A. Leutenegger et al., In-flight verification of the calibration and performance of the ASTRO-H (Hitomi) Soft X-ray Spectrometer. *J. Astron. Telescopes Insrtr. Sci.* **4**, 021407 (2018)
- M..S. Longair, “*High Energy Astrophysics Volume 2 Stars, the Galaxy and the Interstellar Medium*” (Cambridge University Press, 1994)
- K. Makishima et al., X-ray probing of the central regions of clusters of galaxies. *PASJ* **53**, 401 (2001)
- K. Makishima, Plasma phenomena and long distance interaction in space. *J. Phys. Soc. Jpn.* **595**, 63 (2008). ((in Japanese))
- V. Mannings, A..P. Boss, S.S. Russel, “*Protostars and Planets IV*” (The University of Arisona Press, 2000)
- K. Masai, X-Ray emission spectra from ionizing plasmas. *Astrophys. Space Sci.* **98**, 367 (1984)
- C. Meng et al., System design and implementation of the detector assembly of the Astro-H soft x-ray spectrometer. *J. Astron. Telescopes Insrtr. Sci.* **4**, 021404 (2018)
- K. Mitsuda et al., The high-resolution x-ray microcalorimeter spectrometer system for the SXS on ASTRO-H. *Proc. SPIE* **7732**, 773211 (2010)
- K. Mitsuda et al., Soft x-ray spectrometer (SXS): the high-resolution cryogenic spectrometer onboard ASTRO-H. *Proc. SPIE* **9144**, 91442A (2014)
- S.H. Mosley et al., Thermal detectors as x-ray spectrometers. *J. Appl. Phys.* **56**, 1257 (1984)
- NASA’s High Energy Astrophysics Science Archive Research Center, <https://heasarc.gsfc.nasa.gov> (2019)
- H. Noda et al., Thermal analyses for initial operations of the soft x-ray spectrometer onboard the Hitomi satellite. *J. Astron. Telescopes Instr. Sci.* **4**, 011202 (2017)
- M. Oda, “Space Astronomy in Japan”, Third Asian-Pacific Regional Meeting of the International Astronomical Union, edited by M. Kitamura and E. Budding, *Astrophysics and Space Science*, 118 67, (1984)
- T. Ohashi et al., Super DIOS : future x-ray spectroscopic mission to search for dark baryons. *Proc. SPIE* **10699**, 1069928 (2014)

- M. Ozawa et al., Suzaku discovery of the strong radiative recombination continuum of iron from the supernova Remnant W49B. *Astrophys. J.* **706**, L71 (2009)
- D. Porquet et al., He-like ions as practical astrophysical plasma diagnostics: from stellar coronae to active galactic nuclei. *Space Sci. Rev.* **103**, 157 (2010)
- F.S. Porter et al., In-flight performance of the soft x-ray spectrometer detector system on Astro-H. *J. Astron. Telescopes Instrr. Sci.* **4**, 011218 (2017)
- J. I. Read, N. Trentham, “The baryonic mass function of galaxies”, *Philosophical Trans. of The Royal Society A*, 363, 2693 (2005)
- T. Sakurai, Heating mechanisms of the solar corona. *Proc. Jpn. Acad. Ser. B* **93**, 87 (2017). <https://doi.org/10.2183/pjab.93.006>
- J.S. Sanders et al., Deep high-resolution X-ray spectra from cool-core clusters. *MNRAS* **402**, 127 (2010)
- C.L. Sarazin, X-ray emission from clusters of galaxies. *Rev. Modern Phys.* **58**, 1 (1986)
- P. Shirron et al., Design and on-orbit operation of the soft x-ray spectrometer adiabatic demagnetization refrigerator on the Hitomi observatory. *J. Astron. Telescopes Instrr. Sci.* **4**, 021403 (2018)
- D. Sibeck et al., Imaging plasma density structures in the soft X-rays generated by solar wind charge exchange with neutrals. *Space Sci. Rev.* **214**, 79 (2018)
- R.K. Smith et al., “ASTRO-H White Paper - New Spectral Features”, *astro-ph*, [arXiv:1412.1172](https://arxiv.org/abs/1412.1172) (2014)
- R.K. Smith et al., Collisional plasma models with APEC/APED: emission-line diagnostics of hydrogen-like and helium-like ions. *Astrophys. J.* **556**, L91 (2001)
- R.K. Smith, J.P. Hughes, Ionization equilibrium timescales in collisional plasmas. *ApJ* **718**, 583 (2010)
- G. Sneiderman et al., Cryogen-free operation of the Soft X-ray Spectrometer instrument. *J. Astron. Telescopes Instrr. Sci.* **4**, 021408 (2018)
- T. Takahashi et al., Hitomi (ASTRO-H) X-ray astronomy satellite. *J. Astron. Telescopes Instrr. Sci.* **4**, 021402 (2018)
- Y. Takei et al., Vibration isolation system for cryocoolers of soft x-ray spectrometer on-board ASTRO-H (Hitomi). *J. Astron. Telescopes Instrr. Sci.* **4**, 011216 (2017)
- T. Tamura et al., “An X-ray spectroscopic search for dark matter and unidentified line signatures in the Perseus cluster with Hitomi”. *Publ. Astron. Soc. Japan* **71**, 50 (2019)
- Y. Tanaka et al., Gravitationally redshifted emission implying an accretion disk and massive black hole in the active galaxy MCG-6-30-15. *Nature* **375**, 659 (1995)
- M. Tashiro et al., Concept of the X-ray Astronomy Recovery Mission. *Proc. SPIE* **106922** (2018)
- M. Tsujimoto et al., “Status of high resolution X-ray spectrometer SXS onboard ASTRO-H (XVI)”, in *Astronomical Society Japan*, Ehime, Japan, September 15 (2016)
- M. Tsujimoto et al., In-orbit operation of the soft x-ray spectrometer onboard the Hitomi satellite. *J. Astron. Telescopes Instr. Sci.* **4**, 011205 (2017)
- T. Watanabe, Present status of the analysis of X-Ray spectra. *Oyo Buturi* **44**, 116 (1975). (**in Japanese**)
- N. Werner et al., XMM-Newton spectroscopy of the cluster of galaxies 2A 0335+096. *Astron. Astrophys.* **449**, 475 (2006)
- X-IFU Home Page, <http://x-ifu.irap.omp.eu/>
- XRISM Science Team, “Science with the X-ray Imaging and Spectroscopy Mission (XRISM)”, *arXiv: 2003.04962v1* (2020)
- H. Yamaguchi et al., Discovery of strong radiative recombination continua from the supernova remnant IC 443 with suzaku. *Astrophys. J.* **706**, L6 (2009)

**Publisher's Note** Springer Nature remains neutral with regard to jurisdictional claims in published maps and institutional affiliations.